The loss of V0-ATPase induces Microvillus inclusion-like disease in *C. elegans*

Aurélien Bidaud-Meynard[1], Ophélie Nicolle[1], Markus Heck[1] and Grégoire Michaux[1, *]

Univ Rennes, CNRS, IGDR - UMR 6290, F-35000 Rennes, France

* lead contact g.michaux@univ-rennes1.fr

Summary

Food absorption relies on the strong polarity of intestinal epithelial cells and the array of microvilli forming a brush border at their luminal pole. Recent discovery of the genes associated with rare genetic absorption disorders such as Microvillus inclusion disease (MVID) enlightened a major role of membrane trafficking in the maintenance of both the enterocyte polarity and the integrity of the brush border. However, the molecular mechanisms leading to food malabsorption in MVID patients are still poorly understood. Combining genetic RNAi screen and *in vivo* super-resolution imaging in *C. elegans* intestine, we uncovered that depletion of the V0 sector of the V-ATPase (V0-ATPase) fully recapitulates the severe structural, polarity and trafficking defects observed in enterocytes from patients with MVID. Furthermore, we show that V0-ATPase specifically controls an apical trafficking step involving RAB-11 endosomes and the SNARE SNAP-29. Finally, this new *in vivo* MVID model allowed to follow the dynamics of microvillus inclusions and to characterize the potential rescue of MVID phenotype by cholesterol. Hence, we describe a new function for the V0-ATPase in apical trafficking and epithelial polarity maintenance and the promising use of *C. elegans* intestine as an *in vivo* model to better understand the molecular mechanisms of rare genetic enteropathies.

Introduction

Considering that almost all nutrients in the diet are absorbed into blood across the epithelial layer forming the small and large intestinal mucosa (1), proper establishment and maintenance of both the strong polarity of enterocytes and the array of microvilli forming an absorptive brush border at their apical plasma membrane (PM) is essential to ensure intestinal functions. In most of the species, including *C. elegans*, epithelial cells polarity is achieved by actin and microtubule cytoskeleton reorganization, trafficking and signaling-mediated polarized targeting of the CDC-42/PAR-3/PAR-6/PKC-3 (CDC-42/PAR) and Crumbs/PALS1/Patj (CRB) modules at the apical pole and the Dlg/Scribble/Lgl (SCRIB) module at the basolateral pole as well as domain-specific lipids distribution (2). Particularly, CDC-42 has been shown to be a major player of polarity maintenance in *C. elegans* by controlling the apico-basal distribution of PAR proteins (3, 4). The establishment of the brush border, an extended PM surface for efficient nutrient uptake, is thought to be highly dependent on actin cytoskeleton regulating factors which create the force necessary for the onset and maintenance of the microvilli (5-8). Although polarity establishment and brush border formation are early events in intestine development that rely on related trafficking pathways (9-11), glycosphingolipids (GSLs) (12), clathrin and AP-1 (3, 13) and the kinase Lats/WTS-1(14), little is known about their sequential involvement and relationship in establishing and maintaining an absorptive apical PM, especially *in vivo*. For instance, while the brush border component actin crosslinker ezrin (ERM-1 in *C. elegans*) has been proposed to be a major organizer of the intestinal apical PM by recruiting CDC-42 through its Guanine nucleotide exchange factor Dbl3 in mammalian cells (15), its apical localization seems to depend on a Rap2A GTPase-dependent pathway downstream of the PAR protein PAR-4/LKB-1 (16).

Interestingly, some rare genetic absorption diseases recently enlightened a major role of membrane trafficking in the maintenance of both enterocyte polarity and brush border (17).

For instance, Microvillus inclusion disease (MVID, OMIM: 251850) is caused by mutations in the genes coding for myosin-5B (MYO5B) (18), syntaxin-3 (STX3) (19) or Munc18-2/STXBP-2 (STXBP2) (20), three proteins regulating apical trafficking. The major hallmarks of this disease are a microvillus atrophy, the rare formation of microvillus inclusions, as well as a loss of subapical RAB-11^{+} endosomes (17). Additionally, we have recently shown that enterocytes from MVID patients also display mispolarized CDC-42/PAR polarity module (21). At the molecular level, a defective apical PM tethering of RAB-8^{+}/RAB-11^{+} endosomes by Myosin 5B (22) in concert with STX3 (11) and Munc18-2 (20) has been proposed to be the major pathway leading to MVID phenotype (23). However, the molecular mechanism by which these membrane trafficking factors control the integrity of the absorptive apical PM and the other components of this pathway are still unknown. This lack of knowledge may be explained by the fact that essential factors required to build the intestinal apical PM are cytoplasmic proteins, not transported through membrane trafficking *per se*, and by the difficulty to conduct *in vivo* studies in the intestine.

By performing an RNAi screen against a library of trafficking and cytoskeleton factors in the *C. elegans* intestine model, we unveiled that the depletion of the V0 sector of the vacuolar-ATPase (V-ATPase) induces a cytoplasmic and basolateral mislocalization of both PAR polarity module and brush border components. The V-ATPase is a large hetero-multimeric complex (20 subunits in *C. elegans, vha-1* to *vha-18*, *spe-5* and *unc-32*), organized in two main domains: a V1 domain responsible for ATP hydrolysis which provides the energy to the V0 domain, which transports protons (24). The whole V-ATPase complex is responsible for the acidification of intracellular compartments, such as endosomes or lysosomes and plays a major role in PM proteins trafficking (25), while its V0 transmembrane sector (V0-ATPase) has been implicated in the fusion to the yeast vacuole (26) as well as that of synaptic vesicles in drosophila and humans (27, 28), in an acidification-independent manner. In *C. elegans*, the

V0-ATPase subunits *vha-5*, *vha-6* and *vha-19* are required for exosome containing vesicles apical exocytosis in the epidermis (29), intestinal lumen pH regulation (30) and RME-2 receptor trafficking in oocytes (31) but no role in polarity maintenance has been assigned to this complex. In thus study, we describe a new role for the V0-ATPase in apical membrane trafficking necessary for intestinal polarity maintenance and which depletion leads to an MVID-like phenotype in *C. elegans*.

Results

V0-ATPase depletion affects the polarity of brush border and polarity components in the *C. elegans* intestine

To identify new common regulators of polarity and brush border maintenance *in vivo*, we performed a two-steps RNAi screen specifically targeting 408 genes conserved in humans and implicated in membrane trafficking and cytoskeleton regulation in the *C. elegans* intestine. First, we examined the localization of a polarity module component, CDC-42, followed by a second screen with the positive candidates on the localization of ERM-1, a brush border specific actin cross-linker (Table S1). This systematic RNAi screen first confirmed the involvement of clathrin (*chc-1*), AP-1 (*aps-1*) and glycosphingolipids (GSLs) biosynthesis enzymes (i.e. *sptl-1*, *fasn-1*, *pod-2*) (3, 13, 32) in the maintenance of the intestinal polarity (Table S1). This screen also identified several genes along the biosynthetic and endocytic pathways, as well as 10 subunits of the V-ATPase complex (Table S1). Notably, while all the V-ATPase subunits knockdown were found to affect CDC-42 and ERM-1 apical confinement (Fig 1A), only the silencing of the subunits belonging to its V0 transmembrane sector (e.g. *vha-1*) induced a specific basolateral relocalization of ERM-1 and CDC-42 (Fig 1A, middle panel). The decreased apical expression of the V0 subunit VHA-6::mCh by *vha-1(RNAi)* demonstrated the destabilization of the whole V0-ATPase complex by silencing one of its component (Fig S1A-C). Then, this screen was confirmed by silencing several subunits of each V-ATPase sector and studying the localization of endogenously tagged ERM-1, PAR-6 and PKC-3. Consistently, V0- or V1-ATPase subunits knockdown decreased by 15-40% the apical/cytoplasmic ratio of all proteins (Fig 1B-E), which indicates that a V-ATPase acidification-dependent mechanism ensures their apical confinement. Notably, depletion of the V0-ATPase subunits *vha-1*, *-4* and *-19* also induced a basolateral localization of ERM-1, while no basolateral mislocalization was observed upon silencing of the V1-ATPase subunits *vha-8*

and -*15* (Fig 1B, F). Furthermore, PAR-6 and PKC-3 could also be specifically observed at the basolateral PM in ~20% of the enterocytes upon V0-ATPase subunits depletion (Fig 1G). Overall, these data indicate that the V0-ATPase sector specifically controls a sorting step necessary for the polarized localization of both brush border (ERM-1) and polarity module components (PAR-6, PKC-3) in enterocytes, which is consistent with previous studies demonstrating a V0-specific function in various species (26-29).

SNAP-29 is involved in V0-ATPase-mediated polarity maintenance

To identify some of the molecular components of this V0-ATPase-mediated control of intestinal polarity, the effect of V0- or V1-ATPase depletion was assayed on several transmembrane proteins and soluble trafficking factors with a highly polarized expression. First, silencing of subunits from both complexes induced a marginal effect on the cortical confinement of the PM transporters PEPT-1 and SLCF-1, probably due to minor endosomal trafficking defects (Fig 2A, S2A), while the apical expression of the P-glycoprotein PGP-1 was increased upon V1-ATPase silencing (Fig 2B), suggesting that its cellular fate partly depends on a V-ATPase dependent lysosomal degradation, as shown before for the P-glycoprotein ABCB1 in mammalian cells (33). Second, the PM localization of CHC-1/clathrin and the syntaxin SYX-1 (SYN-1) was decreased, while that of the syntaxin UNC-64 (the presumptive mammalian STX3 ortholog) was increased upon all V-ATPase complex subunits depletion (Figs 2C-D and S2B), suggesting a trafficking defect, but no sector-specificity. Notably, none of these highly polarized proteins were observed at the contralateral PM (Figs 2A-E and S2A-B), supporting the notion that the global enterocyte polarity is not compromised upon V0-ATPase depletion. Strikingly, *vha-1/V0-ATPase(RNAi) s*pecifically decreased the apical localization of the soluble N-ethylmaleimide-sensitive factor-attachment protein receptors (SNAREs) component SNAP-29, while *vha-8/V1-ATPase(RNAi)* did not (Fig 2E). SNAP-29

belongs to the SNAP23/25/29 family of SNARE proteins that interact with syntaxins and sec/munc proteins to promote vesicle fusion (34) and its depletion has been shown to affect the endosomes morphology and consequently endocytosis, secretion as well as autophagy pathways (35, 36). This suggests that SNAP-29 is involved in polarity maintenance downstream of V0-ATPase. To test this, the PM localization of ERM-1 was quantified upon *snap-29(RNAi)* (Fig S2C-D). *snap-29* silencing induced a basolateral mislocalization of ERM-1 (Bl/cyto ratio >1.5) in 44.3% of the worms, a population that displayed a mean Bl/cyto ratio of 2.79 (Fig 2F). Hence, these data indicate that SNAP-29 is a downstream target of V0-ATPase polarity maintenance pathway.

High-resolution map of the apical PM revealed that V0-ATPase localizes to microvilli

V0-ATPase has been localized at the apical PM of intestinal epithelia in *C. elegans* (37) and proposed to traffic to the brush border in Caco-2 cells (38). However, conventional confocal imaging in *C. elegans* only allows to determine the apical polarity of markers, but not their precise position regarding the apical PM (i.e. microvilli, terminal web, subapical). The precise localization of the V0-ATPase as well as that of some of the above-mentioned polarity markers was thus assessed by live super-resolution microscopy. This technique confirmed that ERM-1 accumulates in the microvilli, while ACT-5, PGP-1 and SNAP-29 were present at both the microvilli and the underlying terminal web (Fig 2G). Conversely, the PAR component PKC-3 mostly accumulates in the presumptive terminal web. Finally, the V0-ATPase subunit VHA-6 was localized to the microvilli, above the RAB-11 apical staining (Fig 2G). Overall, these results strongly suggest that V0-ATPase localizes at the brush border from where it controls the apical localization of brush border and polarity modules through a trafficking mechanism involving SNAP-29.

V0-ATPase depletion specifically affects the apical recycling pathway

The V-ATPase complex controls the acidification of various endosomes along the biosynthetic and endocytic-recycling routes (39). Using Transmission Electron Microscopy (TEM), we observed the presence of abnormal larger organelles (0.1–0.3 μm in diameter with variable electron density and heterogeneous content) with features of vesicles, lysosomes and autophagosomes upon inhibition of both V0 and V1-ATPase subunits (Fig 3A-B). These "mixed" organelles have been already described in *C. elegans* epidermis and in mammalian cells upon V0-/V1-ATPase silencing or chemical inhibition of V-ATPase complex function, and have been proposed to affect protein sorting along the secretory and lysosomal pathways (29, 40), probably due to an endosome acidification failure. The presence of mixed organelles was confirmed by the accumulation of several endosomal markers in large cytoplasmic structures, including LMP-1 (lysosomes), RAB-7 (late endosomes) and RAB-10 (basolateral recycling endosomes) (Figs 3C and S2F), upon both V0-and V1-ATPase silencing.

Strikingly, V0- but not V1-ATPase depletion let to the specific accumulation of electron-lucent vesicular structures in the cytoplasm (Fig 3D), a hallmark of MVID (41). The number of RAB-5^{+} endosomes was slightly decreased (Fig 3E-F) while RAB-11 virtually disappeared from the apical PM and accumulated in the cytoplasm upon V0- but not V1-ATPase knockdown (Fig 3G-H). Considering that *rab-11* knockdown also induced a basolateral mislocalization of ERM-1 (Fig 3I-J), like *vha-1(RNAi)* or *snap-29(RNAi)* (Fig 1B, F and 2F) and that SNAP-29 localizes on RAB-11-positive recycling endosomes in *C. elegans* intestine (42), likely at the microvilli basis (Fig 2G), this suggests that V0-ATPase controls the enterocyte polarity by regulating a protein recycling step through RAB-11^{+} endosomes in a SNAP-29-dependent manner.

V0-ATPase depletion phenocopies MVID

Next, we asked whether the polarity defects associated with V0-ATPase depletion are associated with brush border structural defects. Combined TEM and super-resolution imaging demonstrated that prolonged V0-ATPase depletion (72 and 96h of *vha-1(RNAi)*) specifically induced a microvillus atrophy, with smaller, thinner or even absent microvilli at the apical PM of enterocytes (Fig 4A-C), while V1-ATPase depletion (*vha-8(RNAi)*), despite inducing a decreased worm size and a mild decrease of microvilli length, did not affect the microvilli structure and organization (Figs 4A-C and S3A). This severe apical PM defect was observed along the whole surface of the deformed lumen and was often associated with a local unhooking of microvilli from the underlying PM (Fig S3B) as well as slightly lengthened adherens junctions (Fig S3C). Finally, super-resolution microscopy allowed to characterize that the brush border components ACT-5 and ERM-1 adopt a pattern reminiscent of microvilli when mislocalized to the basolateral PM (Fig 4D-E). Thus, V0-ATPase depletion specifically leads to severe apical PM structural defects, which may affect the absorptive function of the enterocytes, in line with the accumulation of cellular or bacterial debris in the lumen of *vha-1(RNA)* worms (Fig S3E).

In addition to these apical PM defects, prolonged V0-ATPase depletion leads to the accumulation of rounded ERM-1$^+$ and ACT-5$^+$ structures (Fig 5A-B), which localization displayed a microvilli-like pattern on higher magnification (Fig 5C) and closely resemble cytoplasmic microvillus inclusions (MVIs) observed in MVID patients (43). These structures are also enriched in PKC-3 and SNAP-29 (Fig 5D-E). TEM experiments performed on *vha-1* depleted worms confirmed the presence of typical MVIs lined by inward-pointing microvilli (Fig 5F). We also observed many vacuole-like structures with a wide size (0.1–0.6 μm in diameter), shape and electron-density heterogeneity and containing cellular material (Fig 5G). These vacuole-like structures were positive for the microvilli-specific activated phospho-form

of ezrin, as observed by immuno-EM (Fig 5H) and resemble already described "irregular" MVIs that are probably immature or degrading MVIs (43). Strikingly, microvillus atrophy and MVIs are cellular hallmarks of Microvillus inclusion disease (MVID, OMIM: 251850), a congenital disorder of the intestinal epithelial cells (44) caused by mutations in the genes coding for the trafficking proteins Myosin 5B (MYO5B) (18), Syntaxin3 (STX3) (19) or Munc18-2 (STXBP2)(20). Interestingly, enterocytes of patients with MVID also displayed similar polarity defects, such as a basolateral appearance of microvilli-specific proteins (19), a basolateral mislocalization of PAR polarity module components (21) as well as a cytoplasmic displacement of trafficking (i.e. STX3, the SNAREs family component SNAP23 and cellubrevin) (23) proteins. Finally, MVID has been associated with enlarged lysosomes with heterogeneous content and accumulation of subapical translucent vesicles (43) as well as a specific disorganization of Rab11-positive apical recycling endosomes (45, 46). These and other observations strongly suggest that V0-ATPase depletion in *C. elegans* fully recapitulates the defects observed in the enterocytes of patients suffering from MVID and MVID organoids model (Supplementary Table 2, 3)(47).

Study of MVIs dynamics in *C. elegans* model

Using live microscopy in *Munc18-2* knock-out mouse derived organoids as a MVID model, it has been recently found that MVIs can arise *de novo* in the cytoplasm or by internalization of the apical or basolateral PM (47). To test whether these various modes of MVI onset are conserved in *C. elegans* upon V0-ATPase depletion, we performed live imaging after 96h of *vha-1(RNAi)*. This experiment confirmed that MVIs can rapidly nucleate in the cytoplasm (~3 min) and remain in the cytoplasm from 20 min to more than 90 min (Fig 6A and Movie S1). These structures can also presumably arise by internalization of large ERM-1^{+}structures from the apical and basolateral PM of *vha-1* depleted worms (Fig 6B).

However, little is known about the mechanism leading to the degradation of these structures. It has been proposed that MVIs originate from autophagocytosis of the apical PM, that would ultimately lead to their elimination by lysosomal elimination (48). Furthermore, MVIs induced by *Munc18-2* KO in intestinal organoids are often surrounded by LAMP2$^+$ membranes, and lysosomal remodelling has been proposed to play a role in their nucleation (47). Interestingly, we found that irregular MVIs induced by *vha-1(RNAi)* were often in close proximity to the mixed organelles/lysosomes (Fig 6C) and that some of the ERM-1$^+$ MVIs were also positive for the lysosomal marker LMP-1 (Fig 6D). Furthermore, some MVIs were also surrounded by a second membranous layer positive for ERM-1 (Fig 6E). Considering that i) ezrin has been shown to accumulate at the phagosome membrane and regulate phago-lysosomal fusion (49) and ii) V0-ATPase extinction dramatically activates autophagy, as ascertained by the relocalization of LGG-1::GFP (LC3 *C. elegans* ortholog) from the apical PM to cytoplasmic punctaes (Fig S4) (50), these data strongly suggest that MVIs are eliminated by autophagy-lysosomal in *C. elegans* intestine, as proposed in mammals. This was confirmed by timelapse microscopy on ERM-1$^+$ MVIs surrounded by a second ERM-1$^+$ membrane, which showed the progressive degradation of the MVI inside this structure (Fig 6F and Movie S2).

V0-ATPase depletion-induced MVID-like phenotype can be partly rescued by cholesterol supplementation

Finally, we search for rescue mechanisms of the cellular defects induced by V0-ATPase depletion. Notably, *vha-1(RNAi)* nematodes displayed nearly absent intestinal fat storage granules, compared to control (L4440) or *vha-8(RNAi)* conditions (Fig 7A). A similar phenotype has been observed in *goosepimples/myosin5b* zebrafish mutants (51) and could be reminiscent of lipids and other nutrients absorption defects, as observed in MVID patients. In *C. elegans*, most of the lipids are stored in electron-translucent comportments called lipid

droplets, while cholesterol accumulates in lysosome-related organelles (LROs) (52, 53). Interestingly, V-ATPase knockdown in HeLa cells has been proposed to affect clathrin-mediated endocytosis by inhibiting cholesterol recycling, a phenomenon that was rescued by cholesterol supplementation (54). Furthermore, microvilli are enriched in lipid RAFTs (55) and disruption of these cholesterol-rich structures has been shown to affect microvilli size in polarized MDCK cells (56). Considering that *C. elegans* is auxotroph for cholesterol, trafficking defects observed upon V0-ATPase depletion could create a brush border lipids imbalance, which could lead to MVID-like structural and polarity phenotypes that may be rescued by cholesterol supplementation. To test this conjecture, V0-ATPase depleted worms were cultured on NGM plates supplemented with normal (5 μg.ml-1) or high (50 μg.ml-1) cholesterol concentration. As shown in Figure 7, the microvilli structural defects (Fig 7B) and ERM-1 basolateral mislocalization (Fig 7C) associated with *vha-1* silencing were partly rescued in high-cholesterol compared to control condition. Hence, the MVID phenotype induced by V0-ATPase depletion can be rescued by cholesterol supplementation, which suggests that a lipid homeostasis defect in the brush border may contribute to the polarity and structural defects observed in patients.

Discussion

The V-ATPase complex controls protein trafficking by two different ways. First, its proton-pump activity broadly regulates vesicle acidification of virtually all endosomes, which ensures their maturation and transport capacity (25). Second, its V0 sector plays a more specific and acidification-independent role in vesicle exocytosis in several species, such as the fusion of the yeast vacuole (26) or of synaptic vesicles in drosophila and humans (27, 28). Here, we assigned a new function to the V0-ATPase in the maintenance of the intestinal absorptive PM by ensuring the apical localization of both polarity and brush border components. This essential function of V0-ATPase is further demonstrated by super-resolution and TEM data showing the severe brush border defects as well as the formation of cytoplasmic microvillus inclusions, an extreme phenotype similar to that observed in patients with MVID.

Additionally, we provide compelling evidence that V0-ATPase depletion recapitulates the other polarity, trafficking and structural defects observed in patients with MVID (Supplementary Table 3), including a mispolarization of the CDC-42/PAR polarity module as well as brush border and trafficking proteins, RAB-11 endosomes loss and the accumulation of cytoplasmic vesicles. MVID is a devastating orphan disease with intractable diarrhea and intestinal absorption defects appearing in early life of newborns (44, 57). To date, three genes have been found mutated in MVID (MYO5B, STX3 and STXBP2) (23) and better understanding of the cellular mechanism of this disease will contribute to identify therapeutic avenues, which presently only rely on total parental nutrition or small bowel transplantation (57). *In vitro* cellular models have been developed to study MVID mechanism, based on Myo5B or Rab8/Rab11 depletion or disruption of Myo5B-Rab8/11 interaction (22, 58) as well as patient-derived organoids (17, 19, 47). Furthermore, a zebrafish model carrying a *goosepimples/myosin5b* mutant exhibits some of the structural hallmarks of MVID (51). We describe here for the first time an easy-to-use and genetic screening amenable *in vivo* model

that nearly fully phenocopies the hallmarks of MVID. Even though single deletion of MVID-causing genes seems not to induce an MVID phenotype in *C. elegans* (our unpublished observations), probably due to compensatory mechanisms, we believe that V0-ATPase-depleted nematode is a suitable model to better characterize polarity maintenance mechanisms and pathophysiology.

As a proof of principle, we used *C. elegans* MVID model to characterize some of the protein complexes involved in polarity maintenance that may be affected in patients with MVID. The MVID-like phenotype as a consequence of MVID-causing mutations or V0-ATPase depletion likely rely on a vesicle tethering/fusion deficiency. Indeed, MVID-causing genes belong to the same pathway necessary for the apical PM fusion of recycling endosomes: Myo5B is a molecular motor that interacts with STX3, and Munc-18-2 is a sec/munc family protein that plays an accessory role to help STX3-dependent vesicle tethering (23). Furthermore, other vesicle fusion machinery factors (i.e. SNAP23, Cellubrevin) are mislocalized in MVID models (23). Our data indicate that V0-ATPase controls the intestinal polarity through its vesicle fusion function, in a similar manner than the Myo5b/STX3/Munc18-2 pathway. Indeed, while the whole V-ATPase complex negatively controls UNC-64/STX3 at the apical PM, likely in an acidification-dependent mechanism, the V0 sector maintains the apical polarity by ensuring the apical localization of the SNARE SNAP-29, a member of the SNAP23/25/29 family (59). Interestingly, the direct interaction between the V0-ATPase V0 c-subunit (the ortholog of *vha-1*) and the v-SNARE synaptobrevin (VAMP2) has been shown to be indispensable for efficient synaptic vesicle fusion in mammalian cells (28). Furthermore, the drosophila V0-ATPase subunit V100 (the ortholog of the mammalian V0 a1-subunit) also interacts with the t-SNARE Syx and SNAP25 (27) and V0 a1-subunit has been shown to associate with both synaptic vesicles and presynaptic PM in *T. marmorata*, where it associates with VAMP-2 and the SNAREs complexes (60). Considering

that i) *vha-1(RNAi)* decreased the apical confinement of SNAP-29 and RAB-11, ii) extinction of both proteins induced polarity defects in *C. elegans* intestine, iii) SNAP-29 has been proposed to localize to RAB-11-positive endosomes in *C. elegans* (42) and iv) mammalian SNAP29 might physically interact with STX3 (59), we hypothesize that V0-ATPase directly interacts with SNAP-29 to target the apical exocytosis of RAB-11$^+$ endosomes and may be involved in the same pathway than that of Myo5b/STX3/Munc18-2.

Whether CDC-42/PAR and ezrin/ERM-1, that are not PM integral proteins, are targeted to the apical PM by traversing the RAB-11$^+$ endosomes remains to be explored. Although RAB-11$^+$/RAB-8$^+$ endosomes have been implicated in CDC-42 PM targeting in drosophila and mammalian cells (61, 62), which may be the initial upstream signal for the recruitment of the other PAR components to the apical PM (4), apical sorting of CDC-42/PAR and brush border components may rely on indirect factors that are transported through RAB-11 endosomes, such as scaffolding proteins or lipids. Moreover, while the expression of dominant-negative Rab11 in 3D-grown MDCK affects the apical polarity of the active form of ezrin (63), interactome studies identified a physical interaction between the V-ATPase and ezrin as well as some apically localized scaffolding proteins such as NHERF-1/EBP50/SLC9A3R1 (64). This interaction is consistent with the confined microvilli localization of both ERM-1/ezrin and V0-ATPase (Fig 2). Thus, CDC-42/PAR and ERM-1 apical localization likely relies on both V0-ATPase mediated RAB-11 endosomes exocytosis and protein-protein interactions. Interestingly, we previously showed that depletion of the clathrin adaptor AP-1 induces a polarity inversion of enterocytes in *C. elegans*, that affects the polarized localization of both apical and basolateral PM proteins as well as RAB-11 endosomes, and creates lateral ectopic apical membranes (3). Here, we show that V0-ATPase silencing affects the same endosomes but has a specific effect on brush border and CDC-42/PAR polarity but not on transmembrane proteins (i.e. PEPT-1, PGP-1 and SLCF-1). Interestingly, a similar cargo-selective regulation

has been shown in a CaCo-2 model of MVID, where the apical localization of GLUT5 is affected upon Myo5B or STX3 depletion, but not that of DPPIV (11). The heterogeneous consequence of polarized trafficking disruption may be explained by the tubulo-vesicular structure of recycling endosomes and by the heterogeneous nature of sorting endosomes, which have been shown to target proteins differently in a cytoskeleton- and sorting signals-dependent manner (65) but also by a direct influence of V0-ATPase depletion, which may affect the PM turnover of these proteins via clathrin-mediated endocytosis (54). Furthermore, other pathways have been invoked as critical determinants of intestinal cells polarity maintenance in *C. elegans*, such as the clathrin/AP-1 (3, 13), GSLs (13, 32) and the kinase Lats/WTS-1 (14). Interfering with these pathways induces differential basolateral mislocalization of apically expressed proteins as well as the formation of lateral ectopic membranes but not cytoplasmic MVIs, substantiating the specific function of the V0-ATPase in apical trafficking.

Why ERM-1/ezrin, ACT-5/actin and the CDC-42/PAR module components accumulate at the basolateral PM or cytoplasmic MVIs upon V0-ATPase depletion remains to be elucidated. One possible explanation is the contralateral PM mis-routing of these polarity factors that cannot be delivered to the apical PM, as shown for E-Cadherin upon dominant-negative Rab11 expression (63). Another complementary hypothesis is that the polarized partition of PI(4,5)P_2 and PI(3,4,5)P_3 between the apical and basolateral PM (2), respectively, or the apical enrichment of lipid rafts (66) are defective upon V0-ATPase knockdown, which would result in mispolarized sorting platforms for apical PM proteins. Indeed, the rafts components glycosphingolipids (GSLs) have been shown to play a major role in intestinal cells polarity and luminogenesis (32) and our data indicate that cholesterol rescues V0-ATPase polarity and structural defects (Fig 7).

Besides the mispolarization of brush border and polarity components to the basolateral PM, a key feature of MVID and V0-ATPase knockdown is the formation of cytoplasmic

microvillus inclusions, which contain many apical PM markers. In a recent paper (51) and in the present study (Fig 6), we show that these MVIs may appear by *de novo* nucleation in the cytoplasm or by internalization of the PM. A key step in the onset of these structures may be the failure of apical exocytosis from RAB-11-positive endosomes, which play a major role in apical PM and lumen generation by targeting PAR-3 and activating CDC-42 through the exocyst complex (62). This would result in the sequestration of polarity factors in the cytoplasm that may be sufficient to attract newly-synthesized apical PAR, PM proteins and cytoskeleton and expand a new apical PM in the cytoplasm. Additionally, defective RAB-11 exocytosis may lead to an apical PM protein and lipids homeostasis defect that would create a signal for endocytosis and targeting to autophagosomal-lysosomal degradation, as proposed before (48) and verified in this report (Fig 6). These two non-exclusive possibilities are in accordance with the combined model of MVID mechanism proposed before (17).

Finally, we show that *vha-1* depleted worms lack lipids storages and that cholesterol supplementation partly rescues the polarity and structural defects induced by *vha-1(RNAi)* (Fig 7), which suggests that lipid homeostasis plays a major role in intestinal polarity maintenance, consistent with the effect of GSLs biosynthesis disruption on the intestinal lumen and polarity (13, 32). Interestingly, leucin-derived monomethyl branched-chain fatty acids (mmBCFAs), clathrin and AP-1 have been shown to control the apical PM localization of the V0-ATPase subunit *vha-6* (37), and the GSLs phosphoethanolamine glucosylceramides (PEGC) play a major role in cholesterol mobilization while cholesterol supplementation rescues PEGC deprivation due to glycosylceramide deficiency (67). These data suggest a genetic, physical or functional interaction between these pathways which would be of great interest to characterize.

Several human diseases relying on tissue homeostasis are associated with V-ATPase dysfunction or mutation, such as *cutis laxa* (68, 69) or renal tubular acidosis (70) as well as several cancers (71). Here, we provide compelling evidence that V0-ATPase depletion leads

to MVID in *C. elegans* and could be involved in the aetiology of MVID and other absorption disorders. Complementary use of both *C. elegans*, as a tool to screen for correctors of polarity maintenance defects, such as various lipid-enriched diet, as well as mammalian intestinal organoids or human samples, to confirm the conservation of V0-ATPase function; may lead to a better understanding of rare genetic enteropathies.

Acknowledgements

We thank Verena Gobel, Ken Kemphues, Jeremy Nance, Emily Troemel, Barth Grant and Ken Sato for strains. We also thank the « Biologie de *Cænorhabditis elegans* » facility (UMS3421, Lyon, France) which generated several CRISPR/Cas9 genome edited strains used in this study. Some strains were provided by the CGC, which is funded by NIH Office of research Infrastructure Programs (P40 OD010440; University of Minnesota, USA). We thank A. Perrin for the initial CDC-42 screen. Imaging was performed at the photonic and electron microscopy facilities of the Microscopy Rennes imaging Center (MRiC), Rennes, France. This work was supported by the Ligue Contre le Cancer Grand Ouest [22/29/35/72] and the Fondation Maladies Rares. ABM is the recipient of a postdoctoral fellowship from La Ligue Nationale Contre le Cancer (2017-2018), and a travel grant from the French society for Cell Biology/ITMO BCDE.

Authors contribution

ABM and ON performed and analyzed the experiments. ABM and GM designed the study. ABM wrote the manuscript. GM supervised the study.

Conflict of interest

The authors declare no conflict of interest.

Materials and methods

C. elegans strains and maintenance

Strains were maintained under typical conditions as described (72). When indicated, NGM was supplemented with cholesterol, purchased from Sigma. mNG and mScarlet-tagged ERM-1, UNC-64 and PGP-1 were generated at the « Biologie de *Cænorhabditis elegans* » facility (UMS3421, Lyon, France). The strains used in this study are listed in Supplementary Table S4.

Gene silencing and screening by RNAi

Larval RNAi was performed by feeding as described using the Ahringer-Source BioScience library (3, 73). Briefly, adult hermaphrodites were bleached and transferred to RNAi plates containing HT115 E. coli bacteria expressing the L4440 plasmid alone (control) or encoding the RNAi. Developing worms were kept in RNAi for 72-96h before mounting and imaging. RNAi specificity was verified by sequencing and efficiency by target::GFP signal disappearance, as shown in Figures.

in vivo confocal imaging using *C. elegans*

C. elegans imaging was performed *in vivo* by mounting the worms on a 10% agarose pad in a solution of 100 nm polystyrene microbeads (Polysciences Inc.) to stop worm movement. Confocal observations were performed using a Leica (Wetzlar, Germany) SPE equipped with a 63X, 1.4 NA objective (LAS AF software) or a super-resolution Zeiss LSM880 + Airyscan equipped with a 63X, 1.4 NA objective (Zen Black software). All images were examined using Fiji software.

TEM and immuno-EM

Control and RNAi worms (72-96 hours) were high-pressure frozen with EMPACT-2 (Leica Microsystems) and then freeze substituted in anhydrous acetone containing 1% OsO4, 0.5% glutaraldehyde and 0.25% uranyl acetate for 60 h in a freeze substitution system (AFS-2; Leica Microsystems). Larvae were embedded in Epon-Araldite mix (EMS hard formula). We use

adhesive frames (11560294 GENE-FRAME 65 µL, Thermo Fisher Scientific) for flat-embedding, as previously described (74), more convenient for antero-posterior orientation and sectioning. Ultrathin sections were cut on an ultramicrotome (UC7; Leica Microsystems) and were collected on formvar-coated slot grids (FCF2010-CU, EMS). Each larva was sectioned in 5 different places with ≥ 10 µm between each grid to ensure that different cells were observed. Each grid contains at least 10 consecutive sections of 70 nm. TEM grids were viewed using a JEM-1400 transmission electron microscope (JEOL, Tokyo, Japan) operated at 120 kV, equipped with a Gatan Orius SC 1000 camera (Gatan, Pleasanton, USA) and piloted by the Digital Micrograph program. Micrographs were analyzed using Fiji software.

Immuno-EM

Immuno-electron microscopy was performed as described (75). For ultrathin cryosections and immunogold labeling, larvae were fixed with 4% paraformaldehyde plus 0.1% glutaraldehyde in M9 buffer. Worms were embedded in 12% gelatin and infused in 2.3 M sucrose. Gelatin blocks were frozen and processed for ultracryomicrotomy (UC7cryo; Leica Microsystems). Ultrathin cryosections (80 nm) were double-immunogold labeled and analyzed by TEM as described above. We applied primary antibodies: rabbit phospho-ezrin (Thr567) / radixin (Thr564) / moes (Thr558) (1/100, 3149S Ozyme), detected using protein A conjugated to 10 nm gold particles (PAG, 1/50, CMC, Utrecht, the Netherlands).

Quantification

Apical/cytoplasmic and basolateral/cytoplasmic ratios were calculated by quantifying the signal intensity on a line covering the width of the apical PM and covering at least the length of 2 adjacent intestinal cells. The intensity of the same line was quantified in the cytoplasm underneath the PM. Basolateral ERM-1 appearance was calculated using the Plot Profile function of Fiji, with a R.O.I. of 1.3 µm long crossing the highest basolateral PM intensity. The 5 higher values were kept and divided by the mean fluorescence of the same R.O.I. in the

cytoplasm. Microvilli length and width were quantified using Fiji on 1) TEM pictures on at least 5 sections per worm (Fig 4) or 2) on confocal pictures by calculating the width of at least 4 lines of >100nm long/image (Fig 7).

Statistical analysis

Results are presented as mean ± SEM of the number of independent experiments indicated in the legends, and scattered dots represent individual worms. The total number of larvae used is indicated in brackets in histograms. P values were calculated with the means of at least 3 independent experiments by two-tailed unpaired student's t-test and a 95% confidence level was considered significant. Normal distribution of data and homogeneity of variance were validated by calculating the skew factor (-2 > skew < 2) and the F-test, respectively. Mann-Withney U-test and Welch correction were used for calculating the P-values of non-normal and normal distributions with non-homogenous variances, respectively.

References

1. Kiela PR, Ghishan FK. Physiology of Intestinal Absorption and Secretion. Best Pract Res Clin Gastroenterol. 2016;30(2):145-59.

2. Rodriguez-Boulan E, Macara IG. Organization and execution of the epithelial polarity programme. Nat Rev Mol Cell Biol. 2014;15(4):225-42.

3. Shafaq-Zadah M, Brocard L, Solari F, Michaux G. AP-1 is required for the maintenance of apico-basal polarity in the C. elegans intestine. Development. 2012;139(11):2061-70.

4. Martin-Belmonte F, Gassama A, Datta A, Yu W, Rescher U, Gerke V, et al. PTEN-mediated apical segregation of phosphoinositides controls epithelial morphogenesis through Cdc42. Cell. 2007;128(2):383-97.

5. Heintzelman MB, Mooseker MS. Assembly of the brush border cytoskeleton: changes in the distribution of microvillar core proteins during enterocyte differentiation in adult chicken intestine. Cell Motil Cytoskeleton. 1990;15(1):12-22.

6. Heintzelman MB, Mooseker MS. Structural and compositional analysis of early stages in microvillus assembly in the enterocyte of the chick embryo. Differentiation. 1990;43(3):175-82.

7. Crawley SW, Mooseker MS, Tyska MJ. Shaping the intestinal brush border. J Cell Biol. 2014;207(4):441-51.

8. Saegusa K, Sato M, Sato K, Nakajima-Shimada J, Harada A, Sato K. Caenorhabditis elegans chaperonin CCT/TRiC is required for actin and tubulin biogenesis and microvillus formation in intestinal epithelial cells. Mol Biol Cell. 2014;25(20):3095-104.

9. Apodaca G, Gallo LI, Bryant DM. Role of membrane traffic in the generation of epithelial cell asymmetry. Nat Cell Biol. 2012;14(12):1235-43.

10. Hegan PS, Giral H, Levi M, Mooseker MS. Myosin VI is required for maintenance of brush border structure, composition, and membrane trafficking functions in the intestinal epithelial cell. Cytoskeleton (Hoboken). 2012;69(4):235-51.

11. Vogel GF, Klee KM, Janecke AR, Muller T, Hess MW, Huber LA. Cargo-selective apical exocytosis in epithelial cells is conducted by Myo5B, Slp4a, Vamp7, and STX3. J Cell Biol. 2015;211(3):587-604.

12. Zhang H, Kim A, Abraham N, Khan LA, Gobel V. Vesicular sorting controls the polarity of expanding membranes in the C. elegans intestine. Worm. 2013;2(1):e23702.

13. Zhang H, Kim A, Abraham N, Khan LA, Hall DH, Fleming JT, et al. Clathrin and AP-1 regulate apical polarity and lumen formation during C. elegans tubulogenesis. Development. 2012;139(11):2071-83.

14. Kang J, Shin D, Yu JR, Lee J. Lats kinase is involved in the intestinal apical membrane integrity in the nematode Caenorhabditis elegans. Development. 2009;136(16):2705-15.

15. Zihni C, Munro PM, Elbediwy A, Keep NH, Terry SJ, Harris J, et al. Dbl3 drives Cdc42 signaling at the apical margin to regulate junction position and apical differentiation. J Cell Biol. 2014;204(1):111-27.

16. Gloerich M, ten Klooster JP, Vliem MJ, Koorman T, Zwartkruis FJ, Clevers H, et al. Rap2A links intestinal cell polarity to brush border formation. Nat Cell Biol. 2012;14(8):793-801.

17. Schneeberger K, Roth S, Nieuwenhuis EES, Middendorp S. Intestinal epithelial cell polarity defects in disease: lessons from microvillus inclusion disease. Dis Model Mech. 2018;11(2).

18. Muller T, Hess MW, Schiefermeier N, Pfaller K, Ebner HL, Heinz-Erian P, et al. MYO5B mutations cause microvillus inclusion disease and disrupt epithelial cell polarity. Nat Genet. 2008;40(10):1163-5.

19. Wiegerinck CL, Janecke AR, Schneeberger K, Vogel GF, van Haaften-Visser DY, Escher JC, et al. Loss of STX3 causes variant microvillus inclusion disease. Gastroenterology. 2014;147(1):65-8 e10.

20. Vogel GF, van Rijn JM, Krainer IM, Janecke AR, Posovszky C, Cohen M, et al. Disrupted apical exocytosis of cargo vesicles causes enteropathy in FHL5 patients with Munc18-2 mutations. JCI Insight. 2017;2(14).

21. Michaux G, Massey-Harroche D, Nicolle O, Rabant M, Brousse N, Goulet O, et al. The localisation of the apical Par/Cdc42 polarity module is specifically affected in microvillus inclusion disease. Biol Cell. 2016;108(1):19-28.

22. Knowles BC, Roland JT, Krishnan M, Tyska MJ, Lapierre LA, Dickman PS, et al. Myosin Vb uncoupling from RAB8A and RAB11A elicits microvillus inclusion disease. J Clin Invest. 2014;124(7):2947-62.

23. Dhekne HS, Pylypenko O, Overeem AW, Ferreira RJ, van der Velde KJ, Rings E, et al. MYO5B, STX3, and STXBP2 mutations reveal a common disease mechanism that unifies a subset of congenital diarrheal disorders: A mutation update. Hum Mutat. 2018;39(3):333-44.

24. Lee SK, Li W, Ryu SE, Rhim T, Ahnn J. Vacuolar (H+)-ATPases in Caenorhabditis elegans: what can we learn about giant H+ pumps from tiny worms? Biochim Biophys Acta. 2010;1797(10):1687-95.

25. Maxson ME, Grinstein S. The vacuolar-type H(+)-ATPase at a glance - more than a proton pump. J Cell Sci. 2014;127(Pt 23):4987-93.

26. Baars TL, Petri S, Peters C, Mayer A. Role of the V-ATPase in regulation of the vacuolar fission-fusion equilibrium. Mol Biol Cell. 2007;18(10):3873-82.

27. Hiesinger PR, Fayyazuddin A, Mehta SQ, Rosenmund T, Schulze KL, Zhai RG, et al. The v-ATPase V0 subunit a1 is required for a late step in synaptic vesicle exocytosis in Drosophila. Cell. 2005;121(4):607-20.

28. Di Giovanni J, Boudkkazi S, Mochida S, Bialowas A, Samari N, Leveque C, et al. V-ATPase membrane sector associates with synaptobrevin to modulate neurotransmitter release. Neuron. 2010;67(2):268-79.

29. Liegeois S, Benedetto A, Garnier JM, Schwab Y, Labouesse M. The V0-ATPase mediates apical secretion of exosomes containing Hedgehog-related proteins in Caenorhabditis elegans. J Cell Biol. 2006;173(6):949-61.

30. Allman E, Johnson D, Nehrke K. Loss of the apical V-ATPase a-subunit VHA-6 prevents acidification of the intestinal lumen during a rhythmic behavior in C. elegans. Am J Physiol Cell Physiol. 2009;297(5):C1071-81.

31. Knight AJ, Johnson NM, Behm CA. VHA-19 is essential in Caenorhabditis elegans oocytes for embryogenesis and is involved in trafficking in oocytes. PLoS One. 2012;7(7):e40317.

32. Zhang H, Abraham N, Khan LA, Hall DH, Fleming JT, Gobel V. Apicobasal domain identities of expanding tubular membranes depend on glycosphingolipid biosynthesis. Nat Cell Biol. 2011;13(10):1189-201.

33. Katayama K, Kapoor K, Ohnuma S, Patel A, Swaim W, Ambudkar IS, et al. Revealing the fate of cell surface human P-glycoprotein (ABCB1): The lysosomal degradation pathway. Biochim Biophys Acta. 2015;1853(10 Pt A):2361-70.

34. Sudhof TC, Rothman JE. Membrane fusion: grappling with SNARE and SM proteins. Science. 2009;323(5913):474-7.

35. Sato M, Saegusa K, Sato K, Hara T, Harada A, Sato K. Caenorhabditis elegans SNAP-29 is required for organellar integrity of the endomembrane system and general exocytosis in intestinal epithelial cells. Mol Biol Cell. 2011;22(14):2579-87.

36. Guo B, Liang Q, Li L, Hu Z, Wu F, Zhang P, et al. O-GlcNAc-modification of SNAP-29 regulates autophagosome maturation. Nat Cell Biol. 2014;16(12):1215-26.

37. Zhu H, Sewell AK, Han M. Intestinal apical polarity mediates regulation of TORC1 by glucosylceramide in C. elegans. Genes Dev. 2015;29(12):1218-23.

38. Collaco AM, Geibel P, Lee BS, Geibel JP, Ameen NA. Functional vacuolar ATPase (V-ATPase) proton pumps traffic to the enterocyte brush border membrane and require CFTR. Am J Physiol Cell Physiol. 2013;305(9):C981-96.

39. Forgac M. Vacuolar ATPases: rotary proton pumps in physiology and pathophysiology. Nat Rev Mol Cell Biol. 2007;8(11):917-29.

40. Sobota JA, Back N, Eipper BA, Mains RE. Inhibitors of the V0 subunit of the vacuolar H+-ATPase prevent segregation of lysosomal- and secretory-pathway proteins. J Cell Sci. 2009;122(Pt 19):3542-53.

41. Vogel GF, Hess MW, Pfaller K, Huber LA, Janecke AR, Muller T. Towards understanding microvillus inclusion disease. Mol Cell Pediatr. 2016;3(1):3.

42. Kang J, Bai Z, Zegarek MH, Grant BD, Lee J. Essential roles of snap-29 in C. elegans. Dev Biol. 2011;355(1):77-88.

43. Iancu TC, Mahajnah M, Manov I, Shaoul R. Microvillous inclusion disease: ultrastructural variability. Ultrastruct Pathol. 2007;31(3):173-88.

44. Ruemmele FM, Schmitz J, Goulet O. Microvillous inclusion disease (microvillous atrophy). Orphanet J Rare Dis. 2006;1:22.

45. Vogel GF, Janecke AR, Krainer IM, Gutleben K, Witting B, Mitton SG, et al. Abnormal Rab11-Rab8-vesicles cluster in enterocytes of patients with microvillus inclusion disease. Traffic. 2017;18(7):453-64.

46. Talmon G, Holzapfel M, DiMaio DJ, Muirhead D. Rab11 is a useful tool for the diagnosis of microvillous inclusion disease. Int J Surg Pathol. 2012;20(3):252-6.

47. Mosa MH, Nicolle O, Maschalidi S, Sepulveda FE, Bidaud-Meynard A, Menche C, et al. Dynamic formation of microvillus inclusions during enterocyte differentiation in Munc18-2 deficient intestinal organoids. Cellular and Molecular Gastroenterology and Hepathology. 2018;*in press*.

48. Reinshagen K, Naim HY, Zimmer KP. Autophagocytosis of the apical membrane in microvillus inclusion disease. Gut. 2002;51(4):514-21.

49. Marion S, Hoffmann E, Holzer D, Le Clainche C, Martin M, Sachse M, et al. Ezrin promotes actin assembly at the phagosome membrane and regulates phago-lysosomal fusion. Traffic. 2011;12(4):421-37.

50. Chang JT, Kumsta C, Hellman AB, Adams LM, Hansen M. Spatiotemporal regulation of autophagy during Caenorhabditis elegans aging. Elife. 2017;6.

51. Sidhaye J, Pinto CS, Dharap S, Jacob T, Bhargava S, Sonawane M. The zebrafish goosepimples/myosin Vb mutant exhibits cellular attributes of human microvillus inclusion disease. Mech Dev. 2016;142:62-74.

52. O'Rourke EJ, Soukas AA, Carr CE, Ruvkun G. C. elegans major fats are stored in vesicles distinct from lysosome-related organelles. Cell Metab. 2009;10(5):430-5.

53. Wang P, Liu B, Zhang D, Belew MY, Tissenbaum HA, Cheng JX. Imaging lipid metabolism in live Caenorhabditis elegans using fingerprint vibrations. Angew Chem Int Ed Engl. 2014;53(44):11787-92.

54. Kozik P, Hodson NA, Sahlender DA, Simecek N, Soromani C, Wu J, et al. A human genome-wide screen for regulators of clathrin-coated vesicle formation reveals an unexpected role for the V-ATPase. Nat Cell Biol. 2013;15(1):50-60.

55. Danielsen EM, Hansen GH. Lipid raft organization and function in brush borders of epithelial cells. Mol Membr Biol. 2006;23(1):71-9.

56. Poole K, Meder D, Simons K, Muller D. The effect of raft lipid depletion on microvilli formation in MDCK cells, visualized by atomic force microscopy. FEBS Lett. 2004;565(1-3):53-8.

57. Halac U, Lacaille F, Joly F, Hugot JP, Talbotec C, Colomb V, et al. Microvillous inclusion disease: how to improve the prognosis of a severe congenital enterocyte disorder. J Pediatr Gastroenterol Nutr. 2011;52(4):460-5.

58. Feng Q, Bonder EM, Engevik AC, Zhang L, Tyska MJ, Goldenring JR, et al. Disruption of Rab8a and Rab11a causes formation of basolateral microvilli in neonatal enteropathy. J Cell Sci. 2017;130(15):2491-505.

59. Steegmaier M, Yang B, Yoo JS, Huang B, Shen M, Yu S, et al. Three novel proteins of the syntaxin/SNAP-25 family. J Biol Chem. 1998;273(51):34171-9.

60. Morel N, Dedieu JC, Philippe JM. Specific sorting of the a1 isoform of the V-H+ATPase a subunit to nerve terminals where it associates with both synaptic vesicles and the presynaptic plasma membrane. J Cell Sci. 2003;116(Pt 23):4751-62.

61. Colombie N, Choesmel-Cadamuro V, Series J, Emery G, Wang X, Ramel D. Non-autonomous role of Cdc42 in cell-cell communication during collective migration. Dev Biol. 2017;423(1):12-8.

62. Bryant DM, Datta A, Rodriguez-Fraticelli AE, Peranen J, Martin-Belmonte F, Mostov KE. A molecular network for de novo generation of the apical surface and lumen. Nat Cell Biol. 2010;12(11):1035-45.

63. Desclozeaux M, Venturato J, Wylie FG, Kay JG, Joseph SR, Le HT, et al. Active Rab11 and functional recycling endosome are required for E-cadherin trafficking and lumen formation during epithelial morphogenesis. Am J Physiol Cell Physiol. 2008;295(2):C545-56.

64. Merkulova M, Paunescu TG, Azroyan A, Marshansky V, Breton S, Brown D. Mapping the H(+) (V)-ATPase interactome: identification of proteins involved in trafficking, folding, assembly and phosphorylation. Sci Rep. 2015;5:14827.

65. Puthenveedu MA, Lauffer B, Temkin P, Vistein R, Carlton P, Thorn K, et al. Sequence-dependent sorting of recycling proteins by actin-stabilized endosomal microdomains. Cell. 2010;143(5):761-73.

66. Simons K, Sampaio JL. Membrane organization and lipid rafts. Cold Spring Harb Perspect Biol. 2011;3(10):a004697.

67. Boland S, Schmidt U, Zagoriy V, Sampaio JL, Fritsche RF, Czerwonka R, et al. Phosphorylated glycosphingolipids essential for cholesterol mobilization in Caenorhabditis elegans. Nat Chem Biol. 2017;13(6):647-54.

68. Van Damme T, Gardeitchik T, Mohamed M, Guerrero-Castillo S, Freisinger P, Guillemyn B, et al. Mutations in ATP6V1E1 or ATP6V1A Cause Autosomal-Recessive Cutis Laxa. Am J Hum Genet. 2017;100(2):216-27.

69. Esmail S, Kartner N, Yao Y, Kim JW, Reithmeier RAF, Manolson MF. Molecular mechanisms of cutis laxa- and distal renal tubular acidosis-causing mutations in V-ATPase a subunits, ATP6V0A2 and ATP6V0A4. J Biol Chem. 2018;293(8):2787-800.

70. Imai E, Kaneko S, Mori T, Okado T, Uchida S, Tsukamoto Y. A novel heterozygous mutation in the ATP6V0A4 gene encoding the V-ATPase a4 subunit in an adult patient with incomplete distal renal tubular acidosis. Clin Kidney J. 2016;9(3):424-8.

71. Stransky L, Cotter K, Forgac M. The Function of V-ATPases in Cancer. Physiol Rev. 2016;96(3):1071-91.

72. Brenner S. The genetics of Caenorhabditis elegans. Genetics. 1974;77(1):71-94.

73. Kamath RS, Ahringer J. Genome-wide RNAi screening in Caenorhabditis elegans. Methods. 2003;30(4):313-21.

74. Kolotuev I, Bumbarger DJ, Labouesse M, Schwab Y. Targeted ultramicrotomy: a valuable tool for correlated light and electron microscopy of small model organisms. Methods Cell Biol. 2012;111:203-22.

75. Nicolle O, Burel A, Griffiths G, Michaux G, Kolotuev I. Adaptation of Cryo-Sectioning for IEM Labeling of Asymmetric Samples: A Study Using Caenorhabditis elegans. Traffic. 2015;16(8):893-905.

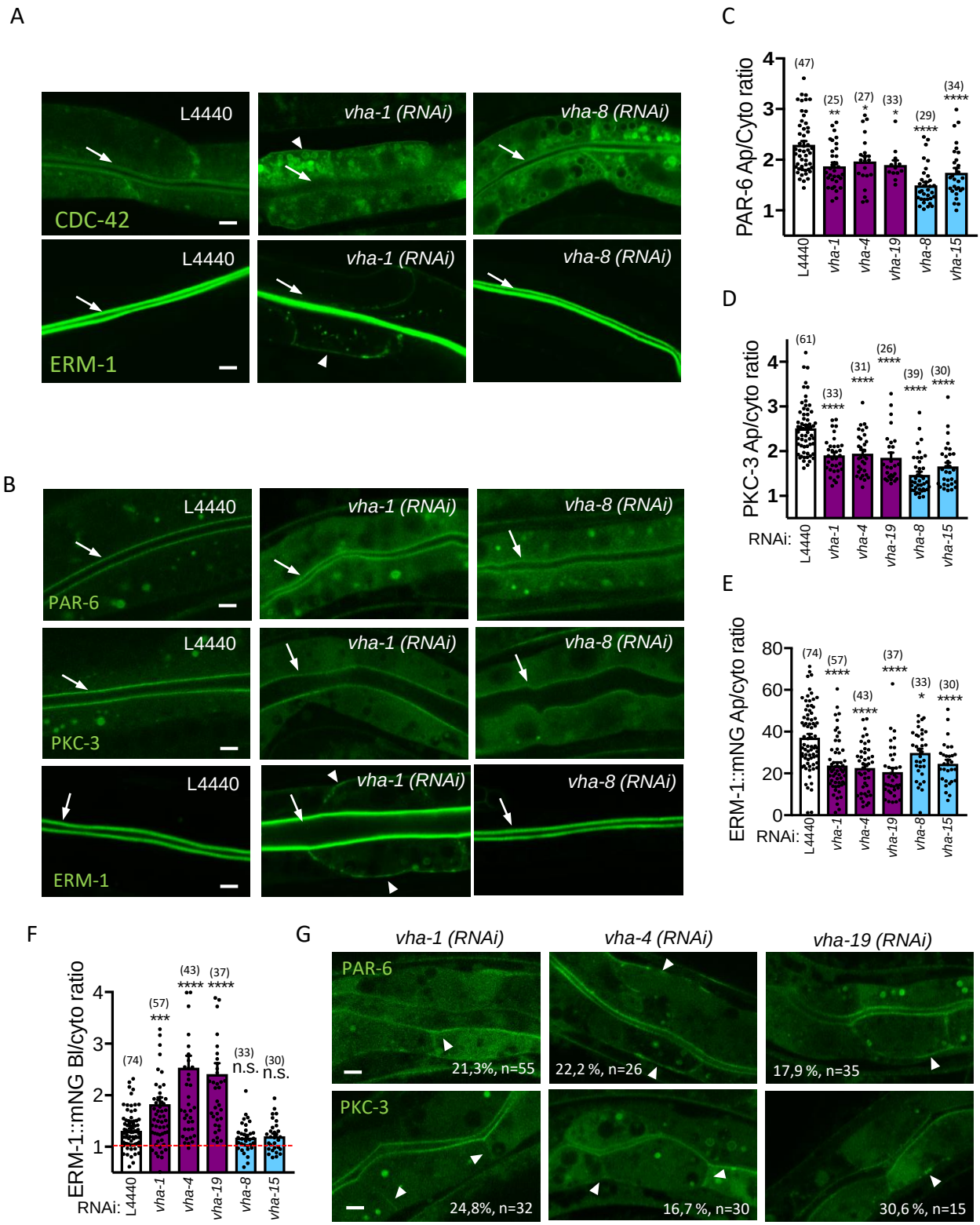
A
L4440
vha-1 (RNAi)
vha-8 (RNAi)
CDC-42
ERM-1
B
PAR-6
PKC-3
C
PAR-6 Ap/Cyto ratio
D
PKC-3 Ap/cyto ratio
E
ERM-1::mNG Ap/cyto ratio
RNAi:
L4440
vha-1
vha-4
vha-19
vha-8
vha-15
F
ERM-1::mNG Bl/cyto ratio
n.s.
G
vha-4 (RNAi)
vha-19 (RNAi)
21,3%, n=55
22,2 %, n=26
17,9 %, n=35
24,8%, n=32
16,7 %, n=30
30,6 %, n=15

Figure 1

Figure 1. V0-ATPase controls the apical localization of polarity and brush border components. (A-C) Larvae expressing exogenous GFP-tagged CDC-42 and ERM-1 (A) or endogenous GFP-tagged PAR-6::GFP, PKC-3::GFP and mNG-tagged ERM (B) were imaged after 72h silencing of V0-ATPase (*vha-1(RNAi))* or V1-ATPase (*vha-8(RNAi))* subunits. Arrows show the intestinal apical PM. Arrowhead show the basolateral mislocalization of markers upon *vha-1(RNAi)*. Scale bar, 5 μm. (C-E) Quantification of the apical/cytoplasmic (Ap/cyto) ratio of PAR-6-GFP (C), GFP-PKC-3 (D) and ERM-1::mNG upon 72h silencing of V0-ATPase (*vha-1*, *-4*, *-19*) or V1-ATPase (*vha-8, -15*) subunits (n=3-5 independent experiments). (F) V0-ATPase subunits (*vha-1, -4, -19*) knockdown specifically induces a basolateral relocalization of ERM-1 mNG (arrowheads). Histogram shows the basolateral/cytoplasmic (Bl/cyto) ratio of ERM-1::mNG. Dotted red line indicates a ratio of 1, which means no basolateral localization. (E) PAR module components are also mislocalized to the basolateral PM upon V0-ATPase knockdown (arrowheads). PAR-6::GFP and GFP::PKC-3 expressing strains were silenced during 72h for the V0-ATPase subunits *vha-1*, *-4* and *-19* and imaged. Arrowheads show the basolateral PM. The percentage of worms displaying basolateral markers and the number of worms analyzed are indicated on each panel. Histograms are mean ± SEM, dots represent individual worms and total number of worms used is indicated in brackets. n.s., non-significant, *p<0.05, **p<0.01, ***p<0.001, ****p<0.0001. Scale bars, 5 μm.

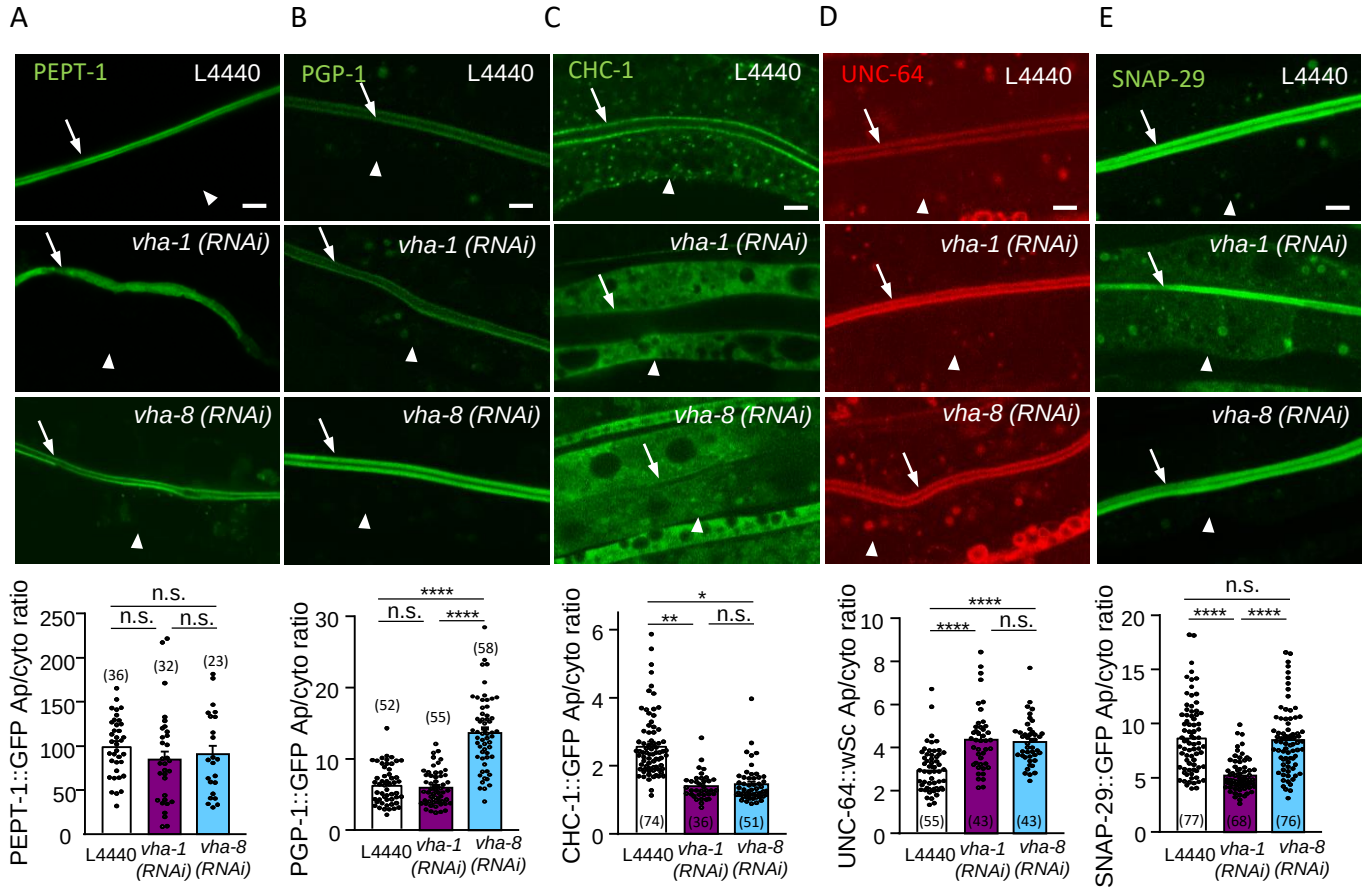
A
B
C
D
E
PEPT-1
PGP-1
CHC-1
UNC-64
SNAP-29
L4440
vha-1 (RNAi)
vha-8 (RNAi)
PEPT-1::GFP Ap/cyto ratio
PGP-1::GFP Ap/cyto ratio
CHC-1::GFP Ap/cyto ratio
UNC-64::wSc Ap/cyto ratio
SNAP-29::GFP Ap/cyto ratio
n.s.
****
*
**
(36)
(32)
(23)
(52)
(55)
(58)
(74)
(36)
(51)
(55)
(43)
(43)
(77)
(68)
(76)
L4440
vha-1 (RNAi)
vha-8 (RNAi)

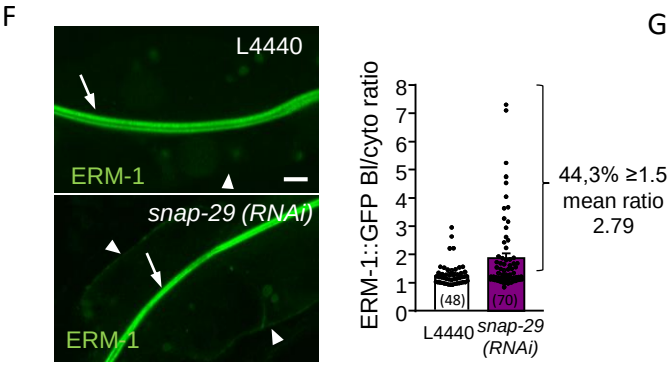
F
L4440
ERM-1
snap-29 (RNAi)
ERM-1
ERM-1::GFP Bl/cyto ratio
(48)
(70)
L4440
snap-29 (RNAi)
44,3% ≥1.5
mean ratio
2.79

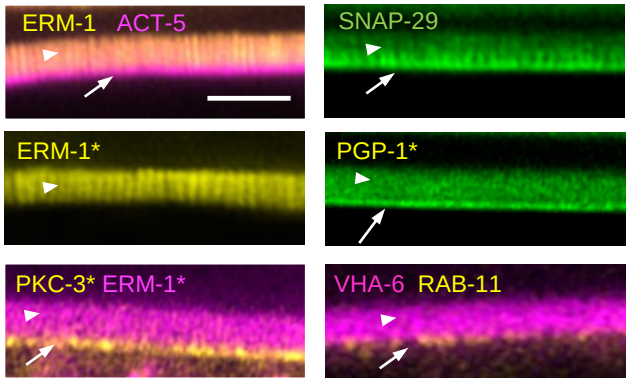
G
ERM-1 ACT-5
SNAP-29
ERM-1*
PGP-1*
PKC-3* ERM-1*
VHA-6 RAB-11

Figure 2

Figure 2. SNAP-29 acts downstream of V0-ATPase in polarity maintenance.
(A-E) V0-ATPase silencing specifically decreases the apical localization of SNAP-29::GFP. Strains expressing the indicated markers were silenced for V0- (*vha-1*) or V1-(*vha-8*) ATPase during 72h and imaged. Histograms represent the quantification of the apical/cytoplasmic (Ap/cyto) ratio of each marker. Arrows and arrowheads indicate the apical and basolateral PM, respectively. (F) *snap-29(RNAi)* induces a basolateral localization of ERM-1. *snap-29* was knocked down by RNAi in ERM-1::GFP-expressing strains and its localization was recorded after 72h. Arrows and arrowheads indicate the apical and basolateral PM, respectively. Right panel represent the quantification of the basolateral/cytoplasmic (Bl/cyto) ratio of ERM-1::GFP. (F) Super-resolution imaging of the apical PM. Strains expressing the indicated markers were mounted and imaged. * indicate endogenously-tagged markers, arrowheads and arrows indicate microvilli and presumptive terminal web, respectively. Scale bars, 5 μm (A-E, F) and 2 μm (G). Histograms are mean ± SEM on each panel, dots represent individual worms and the number of worms used is indicated in brackets.

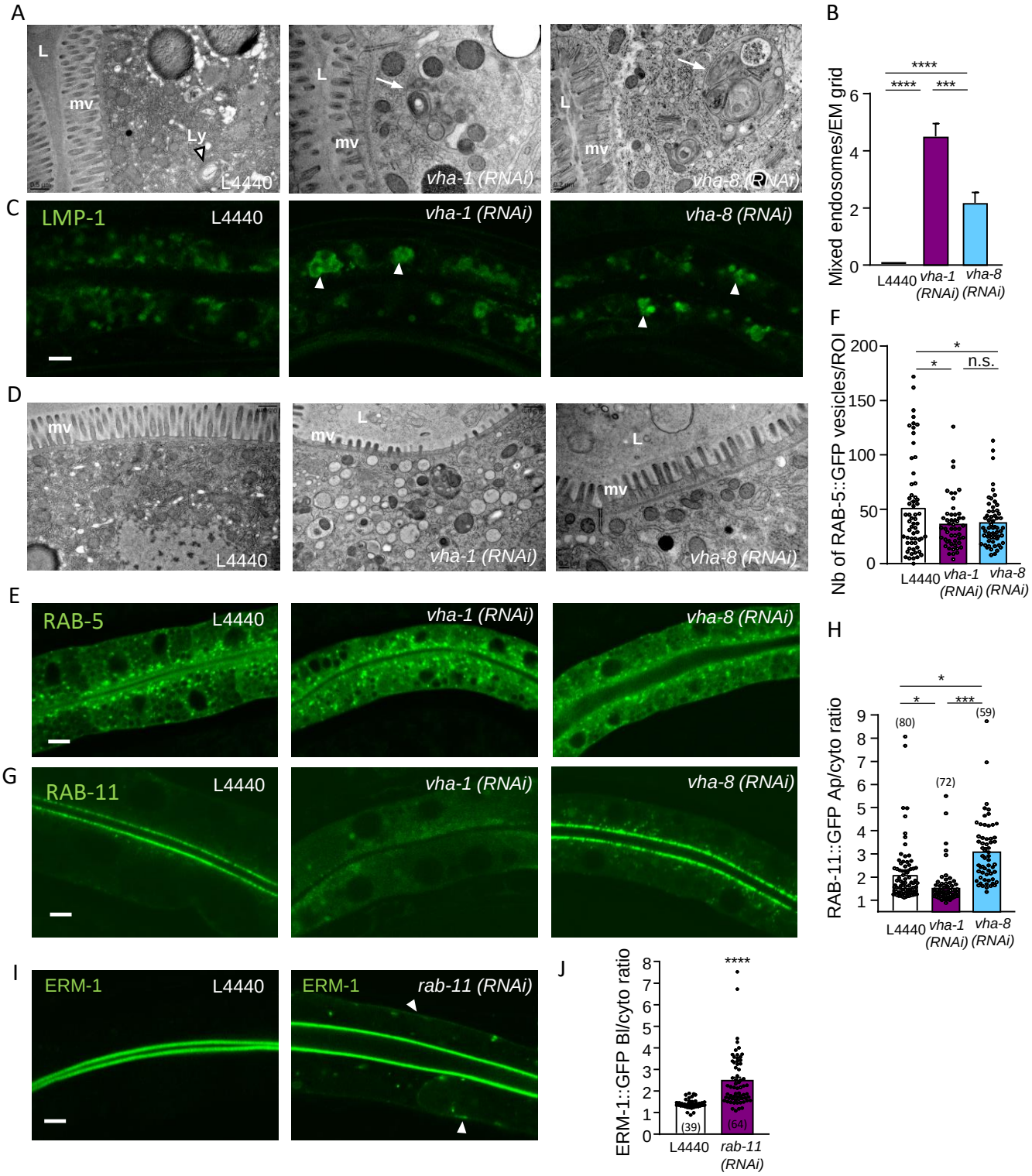
A
L
mv
Ly
L4440
vha-1 (RNAi)
vha-8 (RNAi)
B
Mixed endosomes/EM grid
****
***
L4440
vha-1 (RNAi)
vha-8 (RNAi)
C
LMP-1
L4440
vha-1 (RNAi)
vha-8 (RNAi)
D
mv
L
L4440
vha-1 (RNAi)
vha-8 (RNAi)
F
Nb of RAB-5::GFP vesicles/ROI
*
n.s.
L4440
vha-1 (RNAi)
vha-8 (RNAi)
E
RAB-5
L4440
vha-1 (RNAi)
vha-8 (RNAi)
G
RAB-11
L4440
vha-1 (RNAi)
vha-8 (RNAi)
H
RAB-11::GFP Ap/cyto ratio
(80)
(72)
(59)
L4440
vha-1 (RNAi)
vha-8 (RNAi)
I
ERM-1
L4440
ERM-1
rab-11 (RNAi)
J
ERM-1::GFP Bl/cyto ratio
****
(39)
(64)
L4440
rab-11 (RNAi)

Figure 3

Figure 3. V0-ATPase affects the apical trafficking via RAB-11 apical recycling endosomes.

(A-C) V-ATPase complex silencing affects the morphology of lysosomes. (A) Ultrastructural characterization of transversely-sectioned control (L4440), V0-ATPase (*vha-1*) or V1-ATPase (*vha-8*) depleted worms. While lysosomes with normal morphology and size (~0.5μm) were observed in control worms (left panel, arrowhead), cytoplasmic enlarged "mixed organelles" with distinct lysosomal and vesicular regions were observed upon both *vha-1* and *vha-8(RNAi)* (arrows). (B) Quantification of the number of mixed organelles (n=1-5grid/larvae, n=7-13 larvae). (C) shows the accumulation of the lysosomal marker LMP-1::GFP in large cytoplasmic structures (arrowheads) upon both *vha-1* and *vha-8(RNAi)*. (D) Ultrastructural characterization of transversely-sectioned control (L4440), V0-ATPase (*vha-1*) and V1-ATPase (*vha-8*) depleted worms. Middle panel shows the specific accumulation of cytoplasmic electron-lucent and electron-dense vesicles upon *vha-1(RNAi)*. (E-H) V0-ATPase silencing increases the number of RAB-5^{+} vesicles and specifically disrupts RAB-11^{+} apical recycling endosomes. Confocal imaging of the endosomal markers of apical early/sorting (RAB-5, E) and apical recycling (RAB-11, G) endosomes in control, *vha-1(RNAi)* and *vha-8(RNAi)* conditions (E, G). Quantification of the number of RAB-5+ vesicles (F) and RAB-11 apical/cytoplasmic (Ap/cyto) ratio (H) (n=3). (I-J) *rab-11(RNAi)* phenocopies V0-ATPase depletion on ERM-1::GFP polarity. ERM-1::GFP expressing worms were silenced for *rab-11* and imaged. Arrowheads show the basolateral accumulation of ERM-1. (J) shows ERM-1 basolateral/cytoplasmic (Bl/cyto) ratio quantification (n=3). Histograms are mean ± SEM on each panel, dots represent individual worms and the number of worms used is indicated in brackets. L, lumen; mv, microvilli; Ly, lysosome. Scale bars, 5 μm.

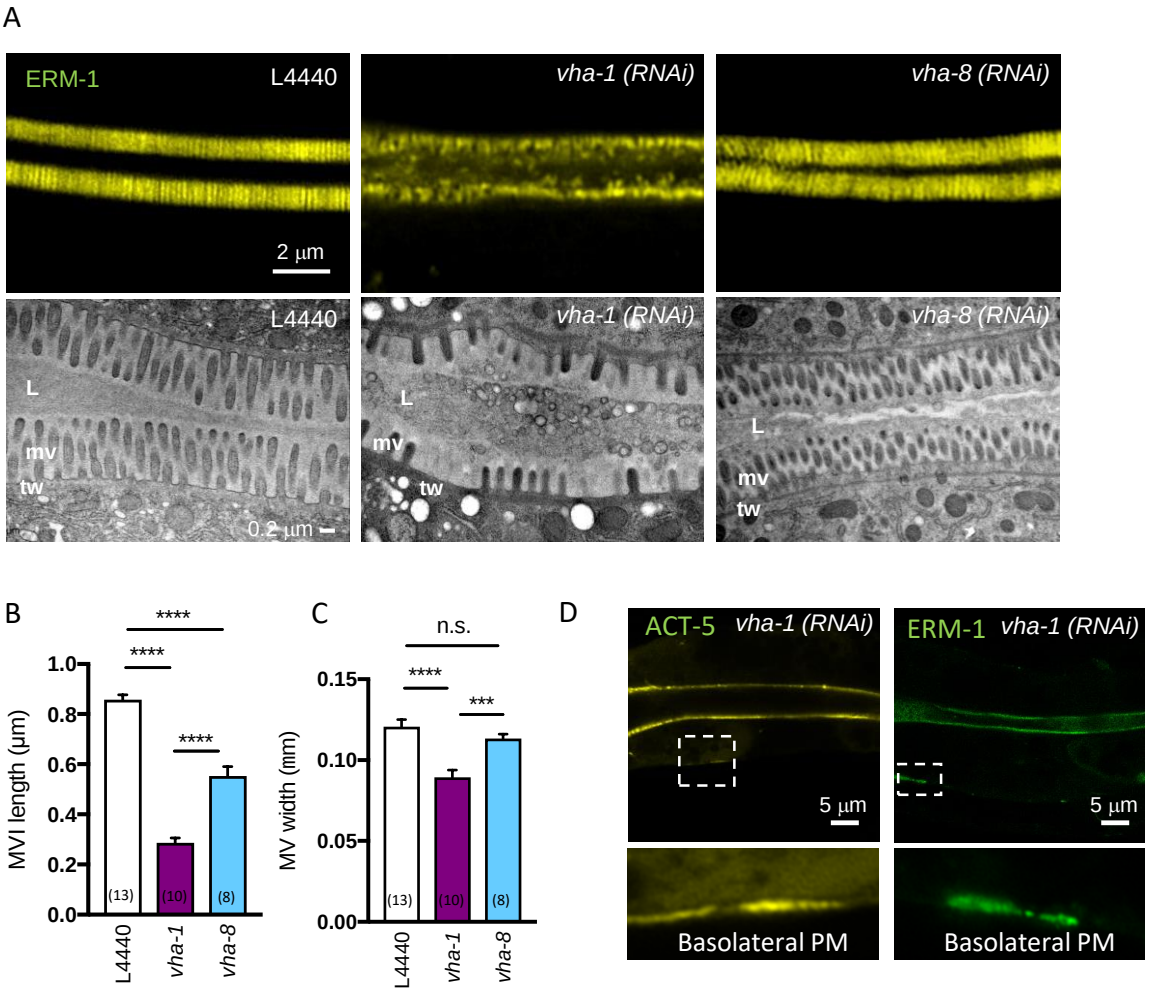
A
ERM-1
L4440
2 µm
vha-1 (RNAi)
vha-8 (RNAi)
L4440
L
mv
tw
0.2 µm
vha-1 (RNAi)
L
mv
tw
vha-8 (RNAi)
L
mv
tw
B
MVI length (µm)
1.0
0.8
0.6
0.4
0.2
0.0
****
****
****
(13)
(10)
(8)
L4440
vha-1
vha-8
C
MV width (mm)
0.15
0.10
0.05
0.00
n.s.
****
***
(13)
(10)
(8)
L4440
vha-1
vha-8
D
ACT-5
vha-1 (RNAi)
5 µm
Basolateral PM
ERM-1
vha-1 (RNAi)
5 µm
Basolateral PM

Figure 4

Fig 4. V0-ATPase depletion induces a microvillus atrophy in *C. elegans*

(A) Precise visualization of microvilli by super-resolution (upper panels) and TEM (lower panels) analysis. Control animals showed the typical intestinal brush border morphology consisting of a dense brush border of microvilli surrounded by a glycocalyx and stabilized by the terminal web, a network of actin and intermediate filaments running below and in parallel to the apical plasma membrane. Conversely, *vha-1(RNAi)* worms display a microvillus atrophy, with irregular, shorter and sparse microvilli, a phenotype that is not observed in *vha-8* depleted worms. Scale bar, X μm. (B-C) Measurement of microvilli length (B) and width (C) upon V0 and V1-ATPase knockdown from TEM images. Data are mean ± SEM, n=5 microvilli/worm on the number of worms indicated in brackets. n.s., non-significant; ****$p<0.0001$. (D) The brush border components ACT-5 and ERM-1 localize to the basolateral PM with a microvilli-like pattern upon 96h *vha-1(RNAi)*. Lower panels are magnified images of the selected areas. L, lumen; mv, microvilli; tw, terminal web.

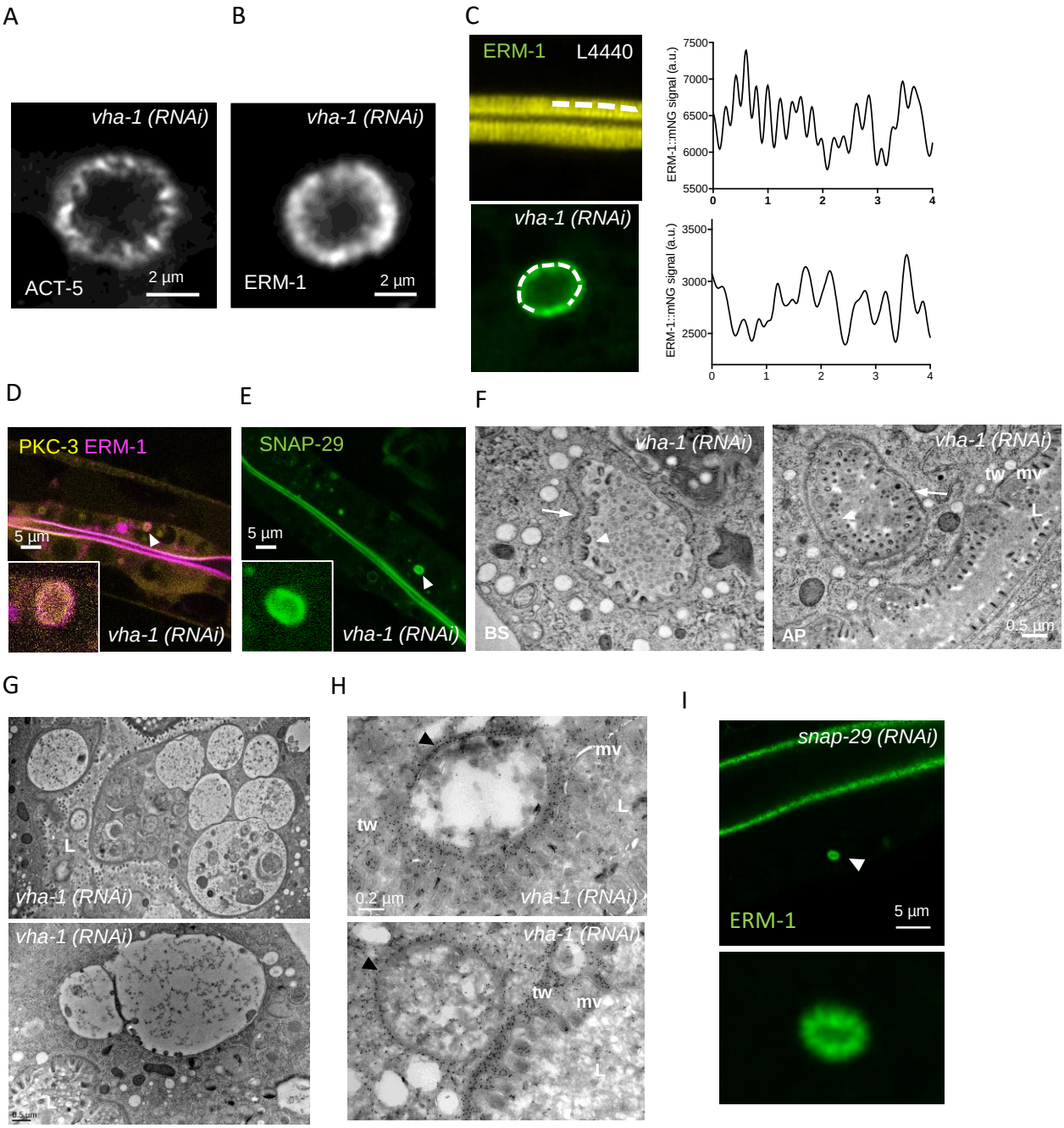
A
vha-1 (RNAi)
ACT-5
2 µm
B
vha-1 (RNAi)
ERM-1
2 µm
C
ERM-1
L4440
vha-1 (RNAi)
ERM-1::mNG signal (a.u.)
7500
7000
6500
6000
5500
0
1
2
3
4
ERM-1::mNG signal (a.u.)
3500
3000
2500
0
1
2
3
4
D
PKC-3 ERM-1
5 µm
vha-1 (RNAi)
E
SNAP-29
5 µm
vha-1 (RNAi)
F
vha-1 (RNAi)
BS
vha-1 (RNAi)
tw
mv
L
AP
0.5 µm
G
L
vha-1 (RNAi)
vha-1 (RNAi)
L
0.5 µm
H
mv
L
tw
0.2 µm
vha-1 (RNAi)
vha-1 (RNAi)
tw
mv
L
I
snap-29 (RNAi)
ERM-1
5 µm

Figure 5

Fig 5. V0-ATPase silencing induces MVID in *C. elegans*

(A-B) 96h V0-ATPase knockdown (*vha-1(RNAi)*) induces the formation of cytoplasmic ERM-1^+ and ACT-5^+ microvillus inclusion-like structures. (C) Line scan shows that rounded structures found in the cytoplasm (lower panel) display similar periodic pattern than that of apical microvilli (upper panel). A line scan of 4 μm was performed (dotted line) on ERM-1::mNG expressing worms apical PM (control worms) and on ERM-1::mNG$^+$ MVI-like structures (96h of *vha-1(RNAi)*). (D-E) GFP::PKC-3 and SNAP-29::GFP localize to 96h *vha-1(RNAi)* induced MVI-like structures. Insert is a magnified image of the structure indicated by the arrowhead. (F-H) V0-ATPase silencing mostly induces cytoplasmic ERM-1^+ vacuoles as well as typical MVIs. (F-G) Ultrastructural analysis of cytoplasmic inclusions observed in *C. elegans* silenced for *vha-1* during 96h by TEM. Note the classical, typical microvillus inclusions showing the symmetrical, mainly inward-pointing arrangement of microvilli (arrowheads) and the area around the inclusion corresponding to the terminal web (arrows). Typical MVIs were found in 3/16 worms. (G) Numerous and larger 'irregular' vacuole-inclusions with a wide heterogeneity in size, shape, and electron-density were found upon 96h *vha-1* silencing. The lumen contains probably amorphous, microvesicular, membranous and lipid components. (H) Immuno-EM analysis of vacuole-like structures using the microvilli and terminal web specific marker phospho-ezrin antibody and nanogold protein A gold in *vha-1(RNAi)* worms (96h) (dark dots). Anti-phospho-ezrin antibody accumulates around *vha-1(RNAi)*-induced vacuole-like structures. (I) *snap-29(RNAi)* (96h) also induces the formation of cytoplasmic ERM-1::mNG$^+$ MVIs. Lower panel is a magnified picture of the MVI indicated by the arrowhead. L, lumen; mv, microvilli; tw, terminal web; AP, apical PM; BS, basal PM.

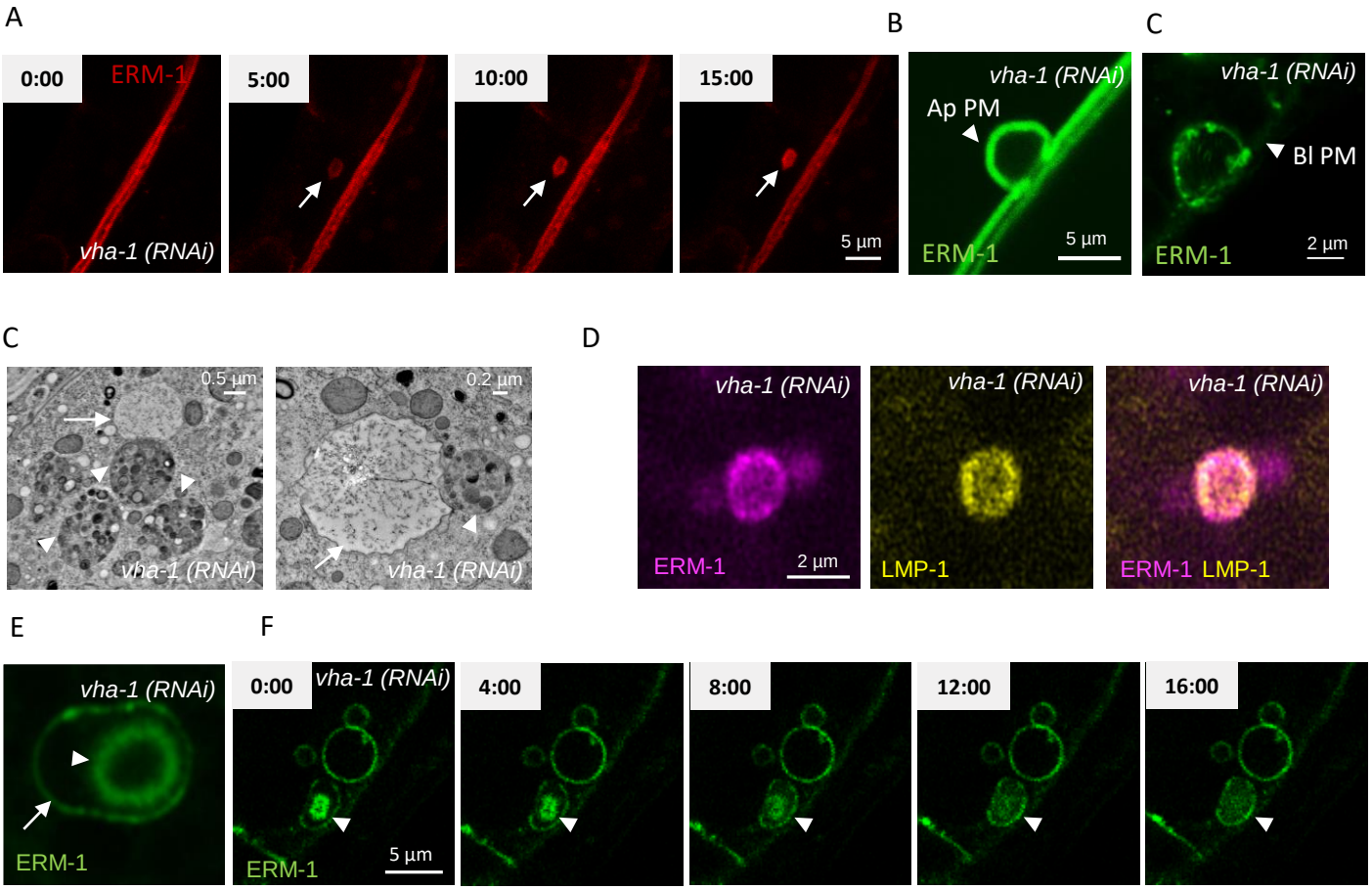
A
0:00
ERM-1
vha-1 (RNAi)
5:00
10:00
15:00
5 µm
B
vha-1 (RNAi)
Ap PM
ERM-1
5 µm
C
vha-1 (RNAi)
Bl PM
ERM-1
2 µm
C
0.5 µm
vha-1 (RNAi)
0.2 µm
vha-1 (RNAi)
D
vha-1 (RNAi)
ERM-1
2 µm
vha-1 (RNAi)
LMP-1
vha-1 (RNAi)
ERM-1 LMP-1
E
vha-1 (RNAi)
ERM-1
F
0:00
vha-1 (RNAi)
ERM-1
5 µm
4:00
8:00
12:00
16:00

Figure 6

Fig 6. Dynamics of microvillus inclusions in *C. elegans*

(A) MVIs cytoplasmic nucleation observed by timelapse imaging in ERM-1::mNG expressing worms silenced for *vha-1* during 96h. Figure shows snapshots every 5 min, MVI is indicated by the arrow. (B) MVIs can arise by internalization of the apical or basolateral PM. ERM-1::GFP and ACT-5::mCh expressing worms were silenced for *vha-1* during 72h and imaged by conventional (B) or super-resolution (C) microscopy. Arrowhead and arrow show the apical and basolateral PM, respectively. (C) MVI-like vacuoles (arrow) are often in the vicinity of lysosomes/mixed-organelles (arrowhead). N2 worms were silenced for *vha-1* during 96h and analyzed by TEM. (D) ERM-1::wSc and LMP-1::GFP colocalize at *vha-1(RNAi)*-induced MVIs (96h). (E-F) 96h *vha-1(RNAi)*-induced MVIs are often surrounded by a second ERM-1^{+} layer in which MVIs are degraded. (E) shows a super-resolution image of MVI (arrowhead) and the surrounding ERM-1^{+} layer (arrow), (F) shows a timelapse imaging of *vha-1(RNAi)*-induced MVI disappearance (image every 4 min).

A

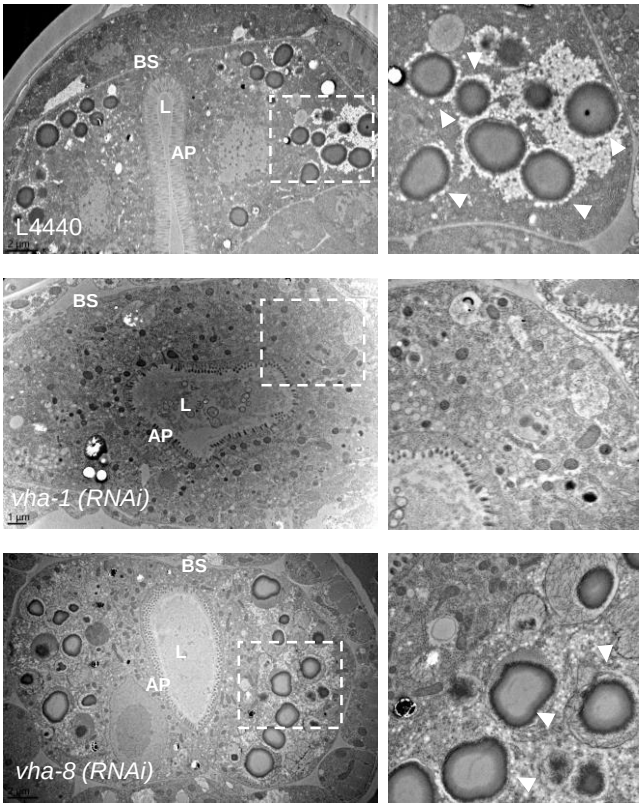
BS
L
AP
L4440
BS
L
AP
vha-1 (RNAi)
BS
L
AP
vha-8 (RNAi)

B

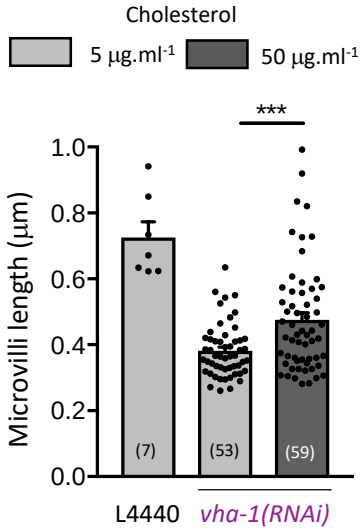
Cholesterol
5 µg.ml-1
50 µg.ml-1
***
Microvilli length (µm)
1.0
0.8
0.6
0.4
0.2
0.0
(7)
(53)
(59)
L4440
vha-1(RNAi)

C

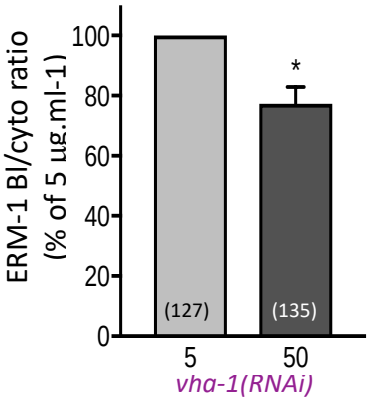
ERM-1 Bl/cyto ratio
(% of 5 µg.ml-1)
100
80
60
40
20
0
*
(127)
(135)
5
50
vha-1(RNAi)

Figure 7

Figure 7. V0-ATPase depletion defects can be counteracted by cholesterol supplementation.

(A) *vha-1* depleted N2 worms, contrary to control or *vha-8*-depleted worms, are devoid of lipid storage granules (arrows). (B-C) Cholesterol supplementation rescues V0-ATPase-induced structural and polarity defects. ERM-1::mNG expressing worms were silenced for *vha-1* and cultured on normal (5 ug.ml-1) or high (50 ug.ml-1) concentration of cholesterol in the NGM medium. (B) Cholesterol supplementation partly corrects the microvillus atrophy induced by V0-ATPase depletion. ERM-1::mNG expressing worms were silenced for *vha-1* during 96h, imaged and the length of the microvilli was measured as described in methods (n=4). (C) Cholesterol decreases the basolateral mislocalization induced by *vha-1(RNAi)*. ERM-1::GFP expressing worms were silenced for *vha-1* during 72h, imaged and the basolateral/cytoplasmic ratio of ERM-1 was quantified (n=5). Histograms are mean ± SEM on each panel, dots represent individual worms and the number of worms used is indicated in brackets. L, lumen; AP, apical PM; BS, basal PM.

A

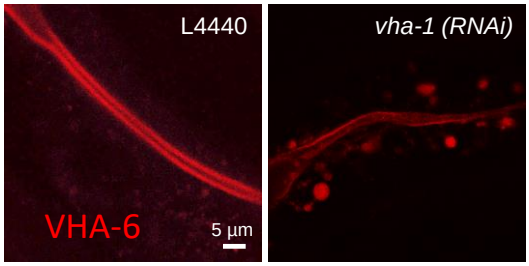

B

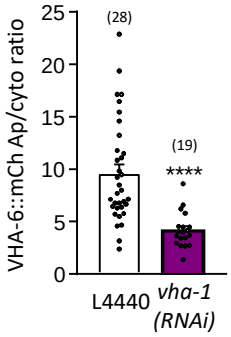

C

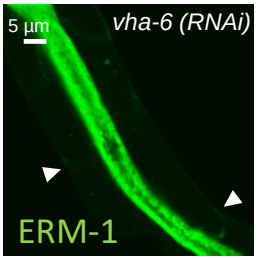

Figure S1

Fig S1. V0-ATPase silencing affects the polarized localization of polarity modules and brush border components.

(A-B) Effect of 72h *vha-1(RNAi)* on the expression of V0-ATPase subunit VHA-6::mCh. (A) shows representative images and (B) the quantification of VHA-6::mCh apical/cytoplasmic ratio (n=3). The histogram shows the mean ± SEM, dots represent individual worms and the number of worms used is indicated in brackets. ****$p<0.0001$. (C) 72h *vha-6(RNAi)* also induces a basolateral mislocalization of ERM-1::GFP (arrow).

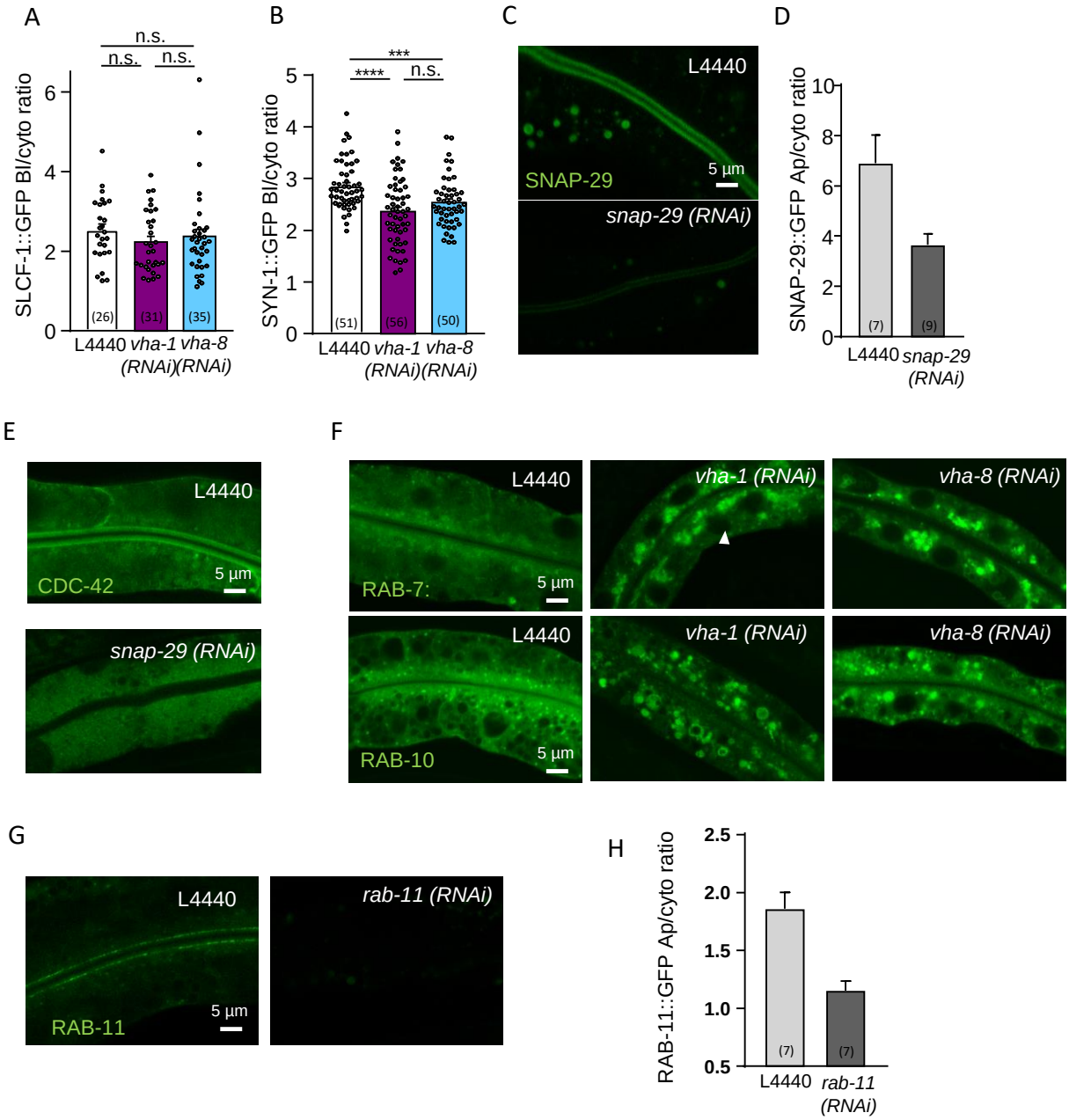
A
n.s.
n.s.
n.s.
SLCF-1::GFP Bl/cyto ratio
0
2
4
6
(26)
(31)
(35)
L4440
vha-1 (RNAi)
vha-8 (RNAi)
B
***
****
n.s.
SYN-1::GFP Bl/cyto ratio
0
1
2
3
4
5
(51)
(56)
(50)
L4440
vha-1 (RNAi)
vha-8 (RNAi)
C
L4440
SNAP-29
5 µm
snap-29 (RNAi)
D
SNAP-29::GFP Ap/cyto ratio
0
2
4
6
8
10
(7)
(9)
L4440
snap-29 (RNAi)
E
L4440
CDC-42
5 µm
snap-29 (RNAi)
F
L4440
RAB-7:
5 µm
vha-1 (RNAi)
vha-8 (RNAi)
L4440
RAB-10
5 µm
vha-1 (RNAi)
vha-8 (RNAi)
G
L4440
RAB-11
5 µm
rab-11 (RNAi)
H
RAB-11::GFP Ap/cyto ratio
0.5
1.0
1.5
2.0
2.5
(7)
(7)
L4440
rab-11 (RNAi)

Figure S2

Fig S2. V0-ATPase polarity maintenance pathway.
(A-B) Effect of 72h V0- or V1-ATPase silencing on the basolateral/cytoplasmic (Bl/cyto) ratio of SLCF-1 and SYN-1. (C-E) *snap-29(RNAi)* decreases SNAP-29::GFP expression and CDC-42::GFP apical localization. (D) represents the apical/cytoplasmic ratio of SNAP-29::GFP. (E) Both *vha-1* and *vha-8(RNAi)* (72h) induce an accumulation of RAB-7 and RAB-10 in large cytoplasmic structures. (G-H) *rab-11(RNAi)* decreases RAB-11 expression. (H) shows the quantification of RAB-11::GFP apical/cytoplasmic ratio. Histograms are mean ± SEM on each panel, dots represent individual worms and the number of worms used is indicated in brackets.

A

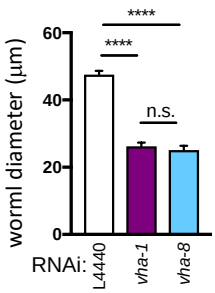

B

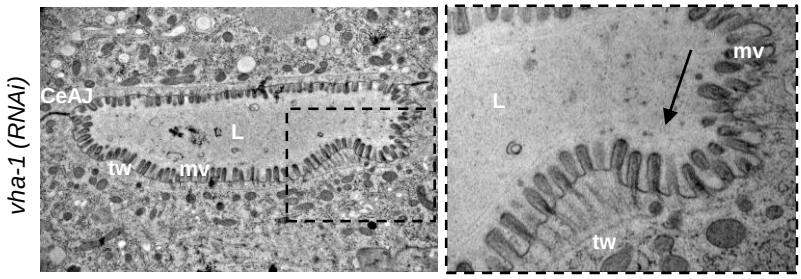

C

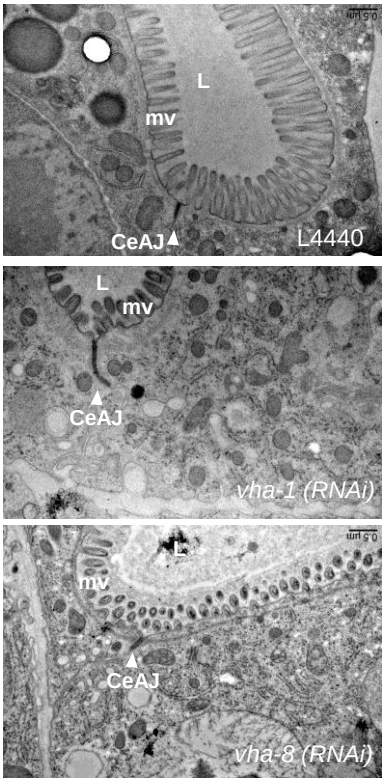

D

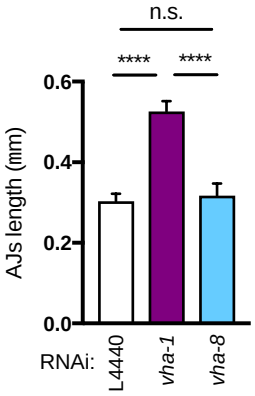

E

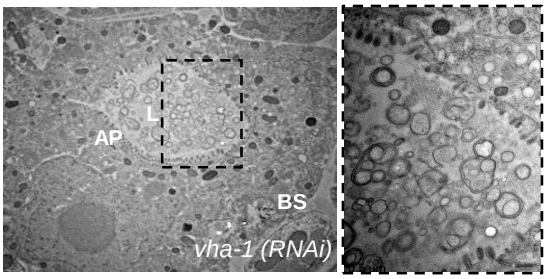

Figure S3

Fig S3. Ultrastructural analysis of V0-ATPase depletion associated defects

(A) V0- or V1-ATPase subunits silencing affects *C. elegans* development. Histogram shows the measurement of the worms diameter from EM images. (B) *vha-1* silencing often induces a detachment of the PM from the terminal web (C) as well as increases the length of cell junctions. Histogram shows the measurement of the electron-dense cell-cell junction length on EM pictures. (E) *vha-1* depleted worms accumulate cell and/or bacterial debris in the intestinal lumen. L, lumen; mv, microvilli; tw, terminal web; AP, apical PM; BS, basal PM; CeAJ, *C. elegans* adherens junctions.

A

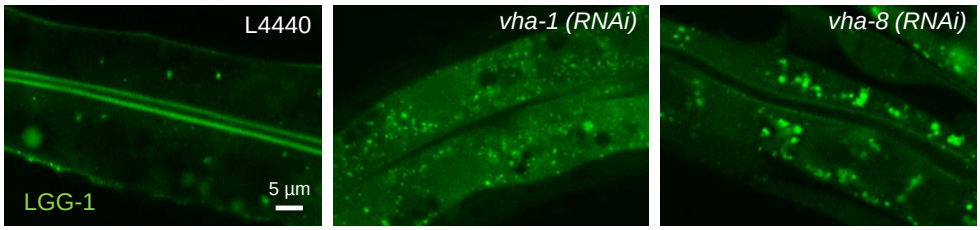
L4440
LGG-1
5 µm
vha-1 (RNAi)
vha-8 (RNAi)

B

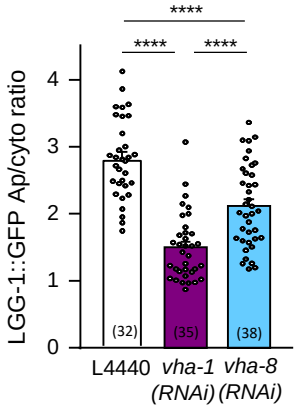
****
****
****
LGG-1::GFP Ap/cyto ratio
0
1
2
3
4
(32)
(35)
(38)
L4440
vha-1 (RNAi)
vha-8 (RNAi)

Figure S4

Figure S4. V-ATPase complex silencing induces autophagy.
(A-B) LGG-1 expressing worms were silenced for *vha-1* or *vha-8* during 72h and imaged. (B) shown the quantification of LGG-1::GFP apical/cytoplasmic (Ap/cyto) ratio. Histograms are mean ± SEM on each panel, dots represent individual worms and the number of worms used is indicated in brackets.

Supplementary Table S1: polarity maintenance screen results

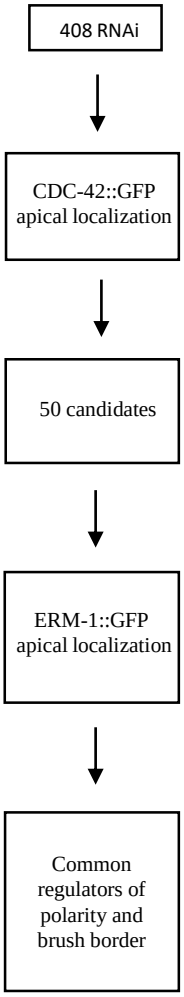

Family	Gene
COPI	E03H4.8
	copb-1
	COPI zeta
	copb-2
	sar-1
Cytoskeleton	erm-1
	act-5
	tba-1
	IFB-1
ECM	noah-1
ER traffic	lpin-1
	phi-26
ESCRTIII	vps-32.1
F ATPase	H28O16.2
GSL	fasn-1
	pod-2
	sptl-1
Membrane fusion	chc-1
	nsf-1
	snap-29
	snap-1
	unc-64
	syx-3
	syx-5
	syx-7
Muscle	mup-4
	let-805
	vab-10
	pat-10
NADPH oxidase	bli-3
Sorting	aps-1
PAR	cdc-42
Rab5	rab-5
Ribosome	rpl-36
V-ATPase	vha-4
	unc-32
	vha-1
	vha-19
	vha-17
	vha-15
	vha-20
	vha-10
	vha-8
	vha-12

Supplementary Table S2: Comparison of *vha-1* and *vha-8* silencing phenotypes

	L4440	***vha-1(RNAi) (V0)***	***vha-8(RNAi) (V1)***
PAR-6, PKC-3, ERM-1 apical PM	Normal	Down	Down
Basolateral PAR-6, PKC-3, ERM-1	No	Yes	No
SNAP-29 cytoplasmic accumulation	No	Yes	No
Mixed organelles	No	Yes	Yes
LMP-1, RAB-7, RAB-10 accumulation	No	Yes	Yes
Accumulation of cytoplasmic lucent vesicles	No	Yes	No
RAB-11 signal	-	Down	Up
Microvillus atrophy	No	Yes	No
MVIs, vacuoles	No	Yes	No

Supplementary Table S3: Comparison of MVID and V0-ATPase depletion phenotypes

	Normal intestine	MYO5B deficient patients	STX3 deficient patients	MUNC18-2 deficient patients (FHL5)	Munc18-2-/- mouse organoids	*vha-1* RNAi *C. elegans*
apical microvilli	normal	microvillus atrophy, severe loss	microvillus atrophy, variable loss	microvillus atrophy, variable loss	microvillus atrophy	microvillus atrophy and dystrophy
microvillus inclusions	no	frequent, observed in 10% of cells	infrequent	infrequent, not fully penetrant	frequent but only after differentiation	infrequent
basolateral microvilli	no	incomplete penetrance	frequent	frequent	frequent but only after differentiation	probable
subapical vesicle accumulation	no	Vesicles and tubulovesicular; variable electron-dense and translucent	Vesicles and tubulovesicular; variable electron-dense and translucent (villus)	electron-dense and translucent vesicles	crypt: translucent villus: translucent tubulovesicular	endosome like vesicles and enlaged vacuolar structures
lysosomal abnormalities	no	Enlarged (auto)lysosomes	Enlarged (auto)lysosomes	high number of lysosomes	enlarged lysosomes	enlarged and high number of lysosomes
STX3 localization	apical membrane	Subapical vesicle and MVIs	reduced/absentprote in level	subapical vesicle and MVIs	diffuse in cytoplasm	Membrane accumulation
F-ACTIN	strong in brush border	Reduced brush border signal, MVIs positive	presence of dot- and ring-like structures	reduced brush border, MVIs stained; variable penetrance and severity	reduced brush border, cytoplasmic foci and MVIs stained	reduced brush border, presence of MVI structures

Supplementary Table S4: *C. elegans* strains used in this study

Srain name	Genotype	Reference
MCP59	*bab59[erm-1::mNG^SEC^3xFlag] I*	This study
MCP64	*erm-1(bab91[erm-1::wrmSc^3xFlag]) I*	This study
FL369	*fgEx13[perm-1::erm-1::gfp + rol-6 (su1006)] ; jyIs17 [vha-6p::mcherry::act-5, ttx-3p::RFP]*	This study
FL316	*dfEx3 [vha-6p::gfp::cdc-42 + rol-6 (su1006)]; unc-119(ed3)III; mcls46 [dlg-1::rfp+unc-119(+)]*	This study
KK1248	*par-6(it319[par-6::GFP]) I*	CGC
KK1228	*pkc-3(it309[GFP::pkc-3]) II*	CGC
GK446	*unc-119(ed3) ; dkIs259[Pact-5-GFP-snap-29 ; Cb.unc-119(+)]*	Sato et al., 2011
FL373	*pkc-3(it309[GFP::pkc-3]) II; erm-1(bab91[erm-1::wrmSc^3xFlag]) I*	This study
MCP113	*bab113[wrmSc^3xFlag::pgp-1] IV*	This study
KWN117	*rnyEx60 [pELA2 (vha-6p:::vha-6::mCherry) + myo-3p::GFP + pCL1 (pha-1+)]*	V. Gobel
FL375	*rnyEx60 [pELA2 (vha-6p:::vha-6::mCherry) + myo-3p::GFP + pCL1 (pha-1+)]; pwIs69 [vha6p::GFP::rab-11 + unc-119(+)]*	This study
KWN246	*pha-1(e2123) III, rnyEx133[opt-2(aa1-412)::GFP) + pha-1(+)]*	CGC
FL368	*bls5[chc-1p::gfp::chc-1 + rol-6(su1006)]; jyls17 [vha-6p::mcherry::act-5, ttx-3p::RFP]*	
MCP91	*unc-64(bab91[wrmSc^3xFlag ::unc-64]) III*	This study
RT258	*pwIs50 [lmp-1::GFP + Cbr-unc-119(+)]*	CGC
RT327	*pwIs72 [vha-6p::GFP::rab-5 + Cbr-unc-119(+)]*	CGC
RT476	*pwIs170 [vha6p::GFP::rab-7 + Cbr-unc-119(+)]*	CGC
RT525	*pwIs206 [vha6p::GFP::rab-10 + Cbr-unc-119(+)]*	CGC
RT311	*pwIs69 [vha6p::GFP::rab-11 + unc-119(+)]*	CGC
VJ268	*fgEx12[pact-5::act-5::gfp]*	Zhang et al., 2012
FL376	*pwIs50 [lmp-1::GFP + Cbr-unc-119(+)]; erm-1(bab91[erm-1::wrmSc^3xFlag]) I*	This study
GK385	*unc-119(ed3) ; dkIs218[Popt-2-GFP-syn-1 ; Cb.unc-119(+)]*	Sato et al., 2011
FS254	*slcf-1(tm2258); Exfs254[slcf-1::gfp]*	Mouchiroud et al., 2010
DA2123	*adIs2122 [lgg-1p::GFP::lgg-1 + rol-6(su1006)]*	CGC